

The use of satellite-measured aerosol optical depth to constrain biomass burning emissions source strength in the global model GOCART

Mariya Petrenko,^{1,2,3} Ralph Kahn,⁴ Mian Chin,⁴ Amber Soja,^{5,6} Tom Kucsera,^{4,7} and Harshvardhan¹

Received 29 March 2012; revised 17 July 2012; accepted 14 August 2012; published 26 September 2012.

[1] Simulations of biomass burning (BB) emissions in chemistry transport models strongly depend on the inventories that define emission source location and strength. We use 13 global biomass burning emission estimates, including the widely used Global Fire Emission Database (GFED) monthly and daily versions, Fire Radiative Power (FRP)-based Quick Fire Emission Data set QFED, and 11 calculated emissions from different combinations of burned area based on the Moderate Resolution Imaging Spectroradiometer (MODIS) products, effective fuel load, and species emission factors as alternative inputs to the global Goddard Chemistry Aerosol Radiation and Transport (GOCART) model. The resultant simulated aerosol optical depth (AOD) and its spatial distribution are compared to AOD snapshots measured by the MODIS instrument for 124 fire events occurring between 2006 and 2007. This comparison exposes the regional biases of each emission option. GOCART average fire AOD values compare best to MODIS-measured AOD when the daily GFED inventory is used as input to GOCART. Even though GFED-based emission options provide the lowest emissions in the tropics, GFED-based GOCART AOD compares best with MODIS AOD in tropical cases. Fire-counts-based emission options give the largest emission estimates in the boreal regions, and the model performs best at higher latitudes with these inputs when compared to MODIS. Comparison of total annual BB emissions by all inventories suggests that burned area estimates are usually the largest source of disagreement. It is also shown that the quantitative relationship between BB aerosol emission rate and model-simulated AOD is related to the horizontal plume dispersion, which can be approximated by the wind speed in the planetary boundary layer in most cases. Thus, given average wind speed of the smoke plume environment, MODIS-measured AOD can provide a constraint to the strength of BB sources at the level of individual plumes.

Citation: Petrenko, M., R. Kahn, M. Chin, A. Soja, T. Kucsera, and Harshvardhan (2012), The use of satellite-measured aerosol optical depth to constrain biomass burning emissions source strength in the global model GOCART, *J. Geophys. Res.*, *117*, D18212, doi:10.1029/2012JD017870.

1. Introduction

[2] Biomass burning (BB) has been recognized as one of the major contributors to carbonaceous aerosol emissions of black carbon (BC) and organic carbon (OC), as well as a source of aerosol precursor gases such as SO₂, NO_x, and a suite of volatile organic compounds [Akagi *et al.*, 2011; Andreae and Merlet, 2001]. Optically and chemically potent biomass burning particles play important roles in atmo-

spheric processes through their impact on air quality [McMurray *et al.*, 2004; Sapkota *et al.*, 2005; Wiedinmyer *et al.*, 2006], visibility [Bäumer *et al.*, 2008; Mazurek *et al.*, 1997] and human health [Seaton *et al.*, 1995], and as one of the factors affecting global climate through direct and indirect radiative effects [Solomon *et al.*, 2007; Lohmann and Feichter, 2005; Yu *et al.*, 2006]. Therefore, it is important to represent biomass burning emissions as accurately as possible in global and regional models, which are among the

¹Department of Earth and Atmospheric Sciences, Purdue University, West Lafayette, Indiana, USA.

Corresponding author: M. Petrenko, Earth Science Directorate, NASA Goddard Space Flight Center, Code 613, Greenbelt, MD 20771, USA. (mshcherb@purdue.edu)

©2012. American Geophysical Union. All Rights Reserved.
10.1029/2012JD017870

²Now at Earth Science Directorate, NASA Goddard Space Flight Center, Greenbelt, Maryland, USA.

³Universities Space Research Association (USRA), Columbia, Maryland, USA.

⁴Earth Science Directorate, NASA Goddard Space Flight Center, Greenbelt, Maryland, USA.

⁵National Institute of Aerospace, Hampton, Virginia, USA.

⁶NASA Langley Research Center, Hampton, Virginia, USA.

⁷Science Systems and Applications, Inc., Lanham, Maryland, USA.

main tools for studying earth and atmospheric processes [Climate Change Science Program Working Group, 2009], estimating climate forcings [Boucher and Anderson, 1995; Dentener et al., 2005; Solomon et al., 2007], and assessing both regional pollution loads [Quinn et al., 2008; Shindell et al., 2008] and long-range transport of pollutants [Chin et al., 2007; Colarco et al., 2004; Damoah et al., 2004; Jaffe et al., 2004; Warneke et al., 2009].

[3] To simulate the emission and subsequent evolution and transport of aerosol particles from fires, models need two essential pieces of information – biomass burning source strength and injection height. Emission injection height is currently an area of active research. Extensive efforts to constrain the atmospheric conditions and fire properties that determine BB emission injection height using plume rise models of different complexity and both satellite and ground-based measurements are described elsewhere and are not addressed in this work [Chen et al., 2009; Freitas et al., 2006; Hyer et al., 2007; Kahn et al., 2007; Sessions et al., 2011; Tosca et al., 2011; Val Martin et al., 2010; M. Val Martin et al., Space-based observations constraints for 1-D plume-rise models, submitted to *Journal of Geophysical Research*, 2012].

[4] Location and strength of BB sources are usually input into the model from an external emission inventory. A number of global and regional BB emission inventories exist, and are usually constructed bottom-up, considering the properties of the burning ecosystem and the extent and properties of the fires [Giglio et al., 2006b; Ito and Penner, 2004; Lioussé et al., 2010; Michel et al., 2005; Turquety et al., 2007; van der Werf et al., 2010; Vermote et al., 2009; Wiedinmyer et al., 2011]. Alternatively, a top-down approach, described, for example, by Dubovik et al. [2008], uses inverse modeling to estimate biomass burning source strength from the measured aerosol properties, such as aerosol optical depth (AOD). This latter approach is labor- and computation-intensive, and is not widely used by the aerosol modeling community.

[5] Natural BB variability [Schultz et al., 2008; van der Werf et al., 2006], errors and uncertainties associated with the estimates and measurements of emission-related parameters, such as (1) burned area [Giglio et al., 2010], (2) biomass type and properties [Fritz and See, 2008], (3) aerosol and gas emission factors [Akagi et al., 2011], (4) properties of the fire and environment in which burning happens [Hyer and Reid, 2009; Soja et al., 2004; van der Werf et al., 2010], as well as (5) different approaches to calculating emissions [Al-Saadi et al., 2008]—all lead to discrepancies between emission estimates provided by BB emission inventories. These discrepancies can be quite significant, and they propagate in aerosol models to impact simulated aerosol effects [Chin et al., 2009; Reid et al., 2009].

[6] The amount of aerosol in the atmospheric column is directly proportional to AOD observed at the top of the atmosphere [Levy et al., 2007, 2010]. AOD is routinely measured by space-borne instruments. Each such measurement captures the aggregation of aerosol particles that have been emitted into the atmosphere by the fires, from the beginning of burning until the time of measurement, except those that were transported away from the field of view. It is, therefore, possible to use satellite-measured AOD as an instantaneous observational constraint on the strength of biomass burning sources in an aerosol model.

[7] In this work, we use 13 global biomass burning emission estimates, including the widely used Global Fire

Emission Database (GFED) monthly and daily versions, Fire Radiative Energy (FRE)-based Quick Fire Emission Data set QFED, and 11 calculated emissions from different combinations of burned area based on the Moderate Resolution Imaging Spectroradiometer (MODIS) products, effective fuel load, and species emission factors as alternative inputs to the global Goddard Chemistry Aerosol Radiation and Transport (GOCART) model. The resultant simulated AOD and its spatial distribution are compared to AOD snapshots measured by the MODIS instrument for 124 fire events occurring between 2006 and 2007, providing information on how satellite AOD data can be used to constrain the BB emission. We describe the approach, emission data sets, GOCART model, and satellite observations in sections 2 and 3, and show the model results of AOD from different emission estimates and discuss the outcome in section 4. Conclusions from this study are given in section 5.

2. Estimation of Biomass Burning Source Strength

2.1. Estimating BB Emissions Based on Burned Area

[8] The most common way to estimate BB emissions is the following empirical relationship, which is based on the one originally introduced by Seiler and Crutzen [1980]:

$$M_j = A * B * \beta * F_j, \quad (1)$$

where M_j is the mass of emitted species j (here BC, OC, and SO_2); A is the burned area; B is the average amount of biomass or organic matter an ecosystem contains per unit area; β is the combustion completeness or burning efficiency, which is the fraction of fuel actually consumed in a fire [Soja et al., 2004; van der Werf et al., 2006] (it is dependent on the fire severity and fuel type and can range from 98% for standing dry grass to less than 10% for dead logs [Lioussé et al., 2004]); and F_j is the emission factor for species j , defined as the amount of species j released per unit of fuel consumed [Andreae and Merlet, 2001], expressed in grams of tracer per kilogram of burned dry mass.

[9] The product of A , B and β in equation (1) represents the amount of fuel consumed within the burned area, or “dry mass burned (DM),” and the product of fuel density B and combustion completeness β the “effective fuel load.” Listed below are several data products that provide estimates of each term in equation (1) individually or as part of a combined quantity, e.g., effective fuel load or dry mass burned. These data products are later combined to provide BB emissions to the aerosol model.

2.1.1. Burned Area (A)

2.1.1.1. The MODIS Collection 5 Burned Area Product: MCD45A1

[10] This product is developed based on the change of surface reflectance following a fire [Roy et al., 2008]. The data are available from the “Reverb” data service (<http://reverb.echo.nasa.gov>) in a set of monthly files, each containing one of the $\sim 10^\circ(\text{lat}) \times 10^\circ(\text{lon})$ granules defined on the MODIS sinusoidal grid [Giglio, 2010]. Each granule contains the locations of burned pixels for each day of the month, at 500 m spatial resolution, which were gridded to the $1^\circ(\text{lat}) \times 1.25^\circ(\text{lon})$ GOCART grid. Burned area

Table 1. GLC2000 Vegetation Types Defined and Their Corresponding Physical Properties and Emission Factors^a

GLC Code	GLC Vegetation Type Description	Fuel Density (kg/m ²)	Burning Efficiency	F _{BC} , g(BC)/ kg(DM)	F _{OC} , g(OC)/ kg(DM)	F _{SO₂} , g(SO ₂)/ kg(DM)
1	Tree Cover broadleaved evergreen	23.35	0.25	0.70	6.40	0.57
2	Tree Cover broadleaved deciduous closed	20.00	0.25	0.60	6.00	1.00
3	Tree Cover broadleaved deciduous open	3.30	0.40	0.62	4.00	0.35
4	Tree Cover needle-leaved evergreen	36.70	0.25	0.60	6.00	1.00
5	Tree Cover needle-leaved deciduous	18.90	0.25	0.60	6.00	1.00
6	Tree Cover mixed leaf type	14.00	0.25	0.60	6.01	0.99
7	Tree Cover regularly flooded fresh water	27.00	0.25	0.70	6.40	0.57
8	Tree Cover regularly flooded saline water	14.00	0.60	0.65	5.15	0.46
9	Mosaic: Tree Cover / Other natural vegetation	10.00	0.35	0.61	5.00	0.68
10	Tree cover, burnt	0	0	0.00	0.00	0.00
11	Shrub Cover closed-open evergreen	1.25	0.90	0.62	4.00	0.35
12	Shrub Cover closed-open deciduous	3.30	0.40	0.62	4.00	0.35
13	Herbaceous Cover closed-open	1.43	0.90	0.62	4.00	0.35
14	Sparse herbaceous or sparse shrub cover	0.90	0.60	0.67	3.11	0.37
15	Regularly flooded shrub and/or herbaceous cover	0	0	0.00	0.00	0.00
16	Cultivated and managed areas	0.44	0.60	0.73	2.10	0.40
17	Mosaic: Cropland / Tree Cover / Other natural v.	1.10	0.80	0.64	3.64	0.36
18	Mosaic: Cropland / Shrub and/or grass cover	1.00	0.75	0.65	3.35	0.37
	Global average GLC ^b			0.64	4.40	0.52
	Global average GFED3 ^c			0.53	4.74	0.62
	Global GOCART			1.0	8.0	1.1

^aReferences: *Lioussse et al.* [2004]; *Michel et al.* [2005]; C. Lioussse, personal communication, 2010.

^bSimple linear averages of emission factors for all GLC vegetation types where F_j are defined.

^cSimple linear averages of GFED3 emission factors for all fire types listed in Table 2.

estimates for the overlapping eight days before and after each month are ignored to avoid duplication. This product is referred to here as “MCD45.”

2.1.1.2. Burned Area Estimated From MODIS Active Fire Counts

[11] This product is based on the 1 km² size fire pixels from the combined MODIS-Terra (MOD14A1) and MODIS-Aqua (MYD14A1) thermal anomalies with multiple counting removed, i.e., pixels classified as fires more than once on the same day are counted only once. These data were obtained from the EOS Clearing House (2009, available at <http://earthdata.nasa.gov/echo>), and the fire counts were gridded to the 1°(lat) × 1.25°(lon) GOCART grid. This product is referred to here as “mod1.”

[12] To estimate the area burned by the detected fires we assume that each pixel classified as burning corresponds to 1 km² of burned area. Here, we have to acknowledge the reported large variations of effective burned area per detected fire, even in the same ecosystem [*Giglio et al.*, 2006b, 2009; *Roy et al.*, 2008; *Soja et al.*, 2004]. The conversion factors reported previously range from 0.3 km² to 6.6 km² effective burned area per fire detection, based solely on MODIS-Terra detection analyses in different locations globally [*Giglio et al.*, 2006b, 2010]. Other estimates include 0.79 km²/pixel [*Soja et al.*, 2009], and 0.625 km²/pixel [*Reid et al.*, 2009]. According to *Soja et al.* [2009], counting every pixel and assuming 1 km²/pixel for every fire detection leads to gross overestimation of burned area (by about a factor of 2 in the western U.S.), highlighting the wide disparity in estimating burned area using fire detection data.

2.1.1.3. Global Fire Emission Data Set Version 3 (GFED3) Burned Area

[13] It is another MODIS-based product with 0.5° × 0.5° spatial and daily temporal resolution [*Giglio et al.*, 2009]. The algorithm combines the detection of change in surface properties (vegetation index) with the use of the active fire

product. Instructions on downloading GFED data and converting burned area from monthly to daily estimates are available from <http://globalfiredata.org/Data/index.html>.

2.1.2. Fuel Density (B) and Effective Fuel Load (B*β)

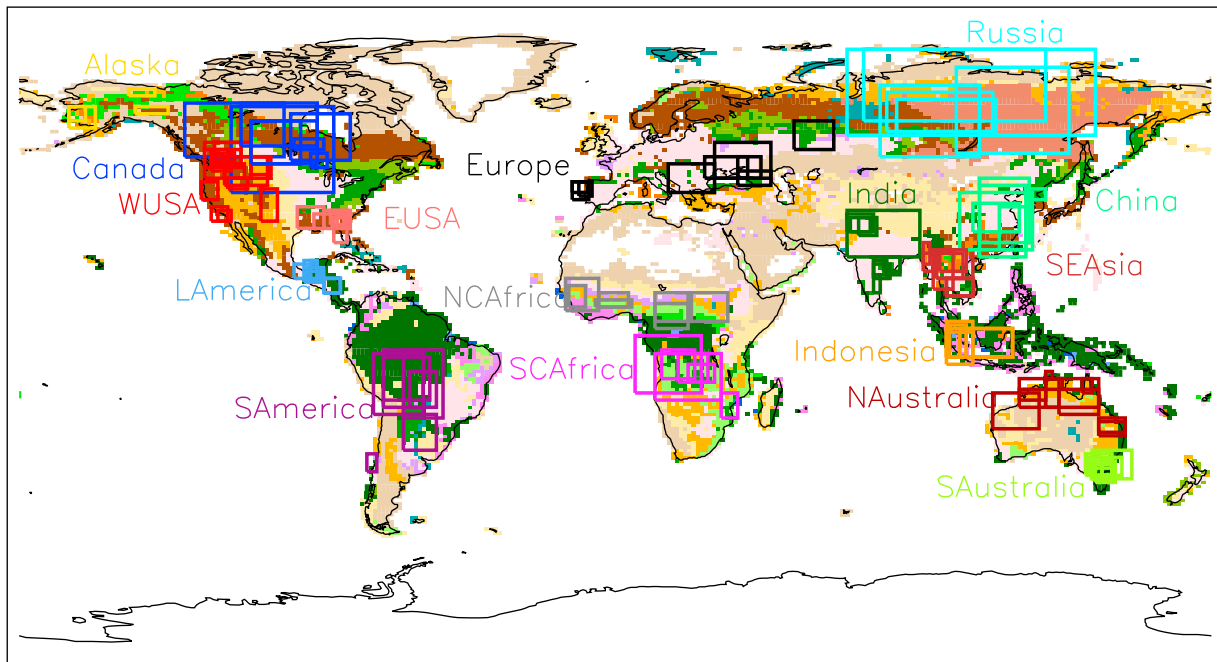
2.1.2.1. Global Land Cover Data Set (GLC2000)

[14] Referred to here as “GLC,” it provides a map of 22 land cover types globally, at the original 1-km and also a 0.5° × 0.5° spatial resolution. GLC methodology and data sets are introduced by *Bartholomé and Belward* [2005] and numerous subsequent publications [e.g., *Gonsamo and Chen*, 2011; *See and Fritz*, 2006; *Xiao-Peng et al.*, 2011], and available online at <http://bioval.jrc.ec.europa.eu/products/glc2000/glc2000.php>. Typical biomass density, combustion completeness, and emission factors are defined for 16 of the 18 vegetated land-cover types [*Lioussse et al.*, 2004, 2010; *Michel et al.*, 2005]. These properties are summarized in Table 1. For comparison, this table also contains global average values of emission factors from all the emission factor options introduced in section 2.1.3 below.

[15] All emission calculations involving the GLC data set were calculated with a spatial resolution of the original data set (0.5° × 0.5°) and then mapped onto the GOCART 1°(lat) × 1.25°(lon) grid. Figure 1 shows the spatial distribution of the vegetation types on the GOCART grid. The vegetation type occupying the largest areal fraction of each grid box is designated as dominant for that box and is the color shown on the map.

2.1.2.2. The Weather- and Ecosystem-Based Fire Emissions (WEB-FE)

[16] It is developed at the National Institute of Aerospace and NASA Langley Research Center, and is available upon request from its developers (A. Soja). In this analysis, we use the Carbon Consumption (CC) database from WEB-FE, which is defined as the potential amount of available carbon consumed by fire.



1 Tree cover, broadleaved, evergreen	10 Undefined
2 Tree cover, broadleaved, deciduous, closed	11 Shrub cover, closed–open, evergreen
3 Tree cover, broadleaved, open	12 Shrub cover, closed–open, deciduous
4 Tree cover, needle–leaved, evergreen	13 Herbaceous cover, closed–open
5 Tree cover, needle–leaved, deciduous	14 Sparse herbaceous or sparse shrub cover
6 Tree cover mixed leaf type	15 Regularly flooded shrub and/or herb. cov
7 Tree cover, regularly flooded, fresh water	16 Cultivated and managed areas
8 Tree cover, regularly flooded, saline water	17 Mosaic: Cropland/Tree cover/other veg
9 Mosaic: tree cover/other natural veg	18 Cropland/Shrub and/or grass cover

Figure 1. The 124 fire cases used in this study, with case boxes color-coded by geographic region. Underlying colors represent the GLC vegetation types described in section 2.1.2.1.

[17] Spatially explicit effective fuel load (defined in the Web-FE project as “fuel consumption”) estimates were first developed for Northern Eurasia based on the amount of fuel contained in ecosystems that could be available to burn [Soja *et al.*, 2004], which is ultimately dependent on the weather that initiates fire events. Unique estimates for the potential amount of carbon (or fuel) consumed are calculated for 35 distinct ecoregions across Northern Eurasia, which includes 4 separate peatland estimates. Fuel data were taken from Alexeyev and Birdsey [1998] and include overstory, understory, litter, peat and soil organic matter. Carbon is assumed to be 50% of the available fuel, and this ratio is used in this study for conversions between carbon consumption and effective fuel load. Each ecoregion estimate consists of 3 potential severity classes, resulting in 105 discrete spatially explicit estimates. For instance, a low-severity surface fire consumes 20% of the accessible understory and litter layer, and a high-severity crown fire consumes 20% of the accessible tree stand vegetation and 100% of the accessible understory and litter are consumed. Ecosystem-based estimates range from low-, medium- to high-severity carbon consumption and have been verified. Subsequently, the data were validated with ground-based fuel consumption data for a range of fire severities and ecosystems ($r^2 = 0.86$). We use the effective fuel load estimate for medium fire severity,

referred to here as “CCm,” as one of the parameters to calculate fire emissions according to equation (1). Medium fire severity is assumed to represent fire properties globally, even though we realize that under- or overestimation of specific fires will occur if they are of high or low severity, respectively.

[18] Global carbon consumption estimates were built from aboveground fuel provided by Olson *et al.* [1985] and soil carbon by Zinke *et al.* [1986], and these global estimates are overlaid with detailed data as they become available (currently for Northern Eurasia, Canada and Alaska). The global estimates were developed for near-real-time use and have proven themselves in numerous field campaigns [e.g., Choi *et al.*, 2008; Pierce *et al.*, 2007]. The information gleaned from this investigation will lead to improvements in this data set.

[19] The effective fuel load from biomass burning events is determined by the fire severity that is associated with the high, medium, and low CC data from WEB-FE. Here we use the Haines index (HI) to estimate the fire severity, which was developed to assess the potential for rapid fire growth [Haines, 1988] and is also known as the Lower Atmosphere Severity Index [Winkler *et al.*, 2007]. The Haines index is a number ranging from 2 to 6 that describes the stability and moisture content of the lower atmospheric layer (~1 km high) with topography taken into account. The index is a

Table 2. GFED3 Emission Factors Used for Different Fire Types, in g Species per kg DM^a

	Deforestation	Savanna and Grassland	Woodland	Extratropical Forest	Agricultural Waste Burning	Peat Fires
BC	0.57	0.46	0.52	0.56	0.48	0.57
OC	4.30	3.21	3.76	9.14	3.71	4.30
SO ₂	0.71	0.37	0.54	1.00	0.40	0.71

^aReference: *van der Werf et al.* [2010].

simple sum of two terms: the lapse rate term (temperature difference between layer bottom and top) describing the stability of the layer, and the dewpoint depression term (difference between temperature and dew point temperature at the lower level). In other words, an unstable, dry atmosphere will have higher HI, indicating a likelihood of more severe fire. The HI was developed, and has been studied most extensively, for North America [*Werth and Ochoa*, 1993; *Winkler et al.*, 2007]; its application has not been evaluated for other parts of the world.

[20] In this study HI was calculated for each GOCART grid box using 3-hourly reanalysis meteorological fields from the Goddard Earth Observing System version 4 Data Assimilation System (GEOS-4 DAS) [*Bloom et al.*, 2005], and the HI value determined the choice of the effective fuel load category from the CC data sets - HI of 2–4, 5, and 6 are associated with the low, medium, and high CC, respectively. These 3-hourly effective fuel load values in each grid box were averaged over the course of 24 h to define the values for a particular day. Effective fuel load estimates calculated using the HI are referred to in this study as “CCi.”

2.1.3. Emission Factors (F_j)

[21] In the standard GOCART configuration, emission factors of 1.0, 8.0, and 1.1 g per kg of burned dry mass are used globally for BC, OC and SO₂, respectively [*Chin et al.*, 2007]. GOCART emission factors are based on the earlier works by *Patterson et al.* [1986] and *Andreae et al.* [1988], which summarize several laboratory and field measurements of F_j 's. The expansion of the body of literature on this subject, recent review publications reporting ecosystem-specific emission factors [*Akagi et al.*, 2011], as well as insights from the current work, will lead to the re-assessment of the emission factor values to be used in the GOCART model.

[22] The GFED emission inventory, introduced below, works with a set of vegetation-type-dependent emission factors based on *Andreae and Merlet* [2001], which are used in some of the GOCART runs together with the GFED dry mass option. For comparison with other inventories, the GFED emission factors for the aerosol-related species of interest are given in Table 2, with the full set of species considered in GFED3, listed by *van der Werf et al.* [2010].

[23] Alternatively, for combinations that include GLC vegetation types, we use vegetation-type-dependent emission factors for BC, OC, and SO₂ provided in the GLC database (Table 1) [*Liousse et al.*, 2004, 2010; *Michel et al.*, 2005].

2.2. Global Fire Emission Data Set (GFED) Emission Estimates

[24] In addition to calculating the emissions from different components, as given in equation (1), we also used emission estimates from GFED version 3 (GFED3), which provides emission amounts ready to use in the models, or burned dry mass estimate ($DM = A*B*\beta$), which can be combined with different emission factor options. The GFED3 daily emission

and burned dry mass at the original $0.5^\circ \times 0.5^\circ$ spatial resolution (<http://www.falw.vu/~gwerf/GFED/GFED3/emissions>) were re-gridded to the $1^\circ(\text{lat}) \times 1.25^\circ(\text{lon})$ GOCART grid. The GFED3 approach to estimating burned area is introduced above in section 2.1.1.3. The Carnegie-Ames-Stanford-Approach (CASA) biogeochemical model used to estimate burned dry mass and emissions is described in detail by *van der Werf et al.* [2010], and the method for scaling monthly GFED3 emissions to daily estimates using MODIS active fire counts is described by *Mu et al.* [2011].

[25] GFED version 2 monthly emission estimates have been widely used in the aerosol modeling community [*Dentener et al.*, 2006], so this data set is considered here to assess the potential changes with the switch to the newer version of GFED.

2.3. Quick Fire Emission Data Set (QFED) Based on Fire Radiative Energy (FRE)

[26] The relationship between the energy released by the fire and emission of aerosols and gases was suggested by *Kaufman et al.* [1996], and has subsequently been studied and refined [*Ichoku and Kaufman*, 2005; *Schroeder et al.*, 2010; *Vermote et al.*, 2009; *Wooster*, 2002; *Wooster et al.*, 2005]. The approach presented by *Wooster* [2002] and *Wooster et al.* [2005] relates the amount of combusted biomass, which is equivalent to the term “dry mass burned (DM)” used in this study, and fire radiative energy (FRE) as follows:

$$DM(\text{kg}) = a * \text{FRE} (\text{MJ}), \quad (2)$$

where a is an empirically derived factor. Fire radiative energy is the fire radiative power (FRP) obtained from the $3.9 \mu\text{m}$ wavelength radiative energy flux at the top-of-atmosphere measured by MODIS, and integrated over time for the estimated duration of burning. This relationship has been used to estimate the amount of DM from the MODIS FRE, and the limitations of using measurements in the satellite thermal channels for detecting and characterizing fires, have been discussed by the developers of FRE-based emission inventories, such as Global Fire Assimilation System (GFAS [*Kaiser et al.*, 2012]) and Quick Fire Emission Data set (QFED (A. Darmenov and A. da Silva, manuscript in preparation, 2012)). Species-specific emission factors are then applied to DM estimates to obtain aerosol emissions. QFED developers omit the DM estimation step and work directly with GFED emissions (using CO as a reference) to find coefficients that relate emission rates to FRP.

[27] After the initial emissions have been estimated, these estimates are adjusted to improve the agreement between MODIS-measured AOD and model-simulated AOD by running multiple regression while considering BB and anthropogenic AOT components as independent variables, whereas AOD for other aerosol types (dust, sea salt,

volcanic, etc.) are kept unchanged. The regression parameters of modeled total AOD on MODIS AOD for different biomes and regions provide the coefficients needed to tune the QFED emissions on a per-region basis (Darmenov and da Silva, manuscript in preparation, 2012). QFED is the default BB emission inventory in the GEOS-5 modeling system [Rienecker *et al.*, 2008]. It provides daily estimates of BB emissions at $\sim 0.25^\circ(\text{lat}) \times 0.3125^\circ(\text{lon})$ horizontal resolution, and can be obtained from its developers at the Global Modeling and Assimilations Office (GMAO, <http://gmao.gsfc.nasa.gov/>) at NASA Goddard Space Flight Center. Since QFED calculates emissions based on a different approach from the other emission options used in this study, we consider it a valuable contribution to the comparison of annual emission estimates. However, because QFED emissions are adjusted to better reproduce the MODIS AOD, QFED-based GOCART runs are not used in model evaluations with MODIS AOD described in sections 4.2–4.4.

2.4. BB Emission Options

[28] Ready-to-use emission inventories and the combinations of parameters, as described above, resulted in 13 data sets that define BB source location and strength. These products are referred to here as “emission options,” and are summarized in Table 3. The name of the emission option is usually composed of three parts, where the first set of alphanumeric symbols stand for burned area product, next set of symbols signify the effective fuel load product, and the last symbols define the emission factor option. If the emissions came from a ready-to-use inventory (such as GFED3 or QFED), the name of the inventory is kept unchanged.

3. Aerosol From Satellite Observations and Model Simulations

3.1. GOCART Model

[29] GOCART is a global chemistry and transport model that simulates the major tropospheric aerosol types: sulfate and its precursors, OC, BC, dust, and sea salt. For this work, it uses assimilated meteorological fields from the GEOS-4 DAS [Bloom *et al.*, 2005] with a spatial resolution of 1.25° longitude by 1° latitude, and 30 vertical layers. The time step of model output is 3 h.

[30] The GOCART model is described in detail in several publications [e.g., Chin *et al.*, 2000, 2002, 2007, 2009; Ginoux *et al.*, 2001]. Briefly, chemical processes in the model include gas and liquid phase reactions that convert sulfate precursors (dimethylsulfide or DMS, and SO_2) to sulfate. Carbonaceous aerosol aging is represented by the conversion of hydrophobic aerosols (original 80% of BC and 50% of OC) to hydrophilic with an e-folding time of 2 days. Physical processes include aerosol emission, advection, convection, as well as wet and dry deposition. Anthropogenic emissions are input from available global inventories as described by Chin *et al.* [2009]. Annual anthropogenic emissions of SO_2 , BC, and OC are provided by Streets *et al.* [2009]. Other anthropogenic emissions include ship and aircraft emissions databases (Eyring *et al.* [2005] for international ship emission; Mortlock and Van Alstyne [1998] for aircraft emissions from the Atmospheric Effects of Aviation Project database). Natural emissions are either from available

estimates or calculated online as a function of meteorological conditions.

[31] Biomass burning emissions of SO_2 , BC, and OC are provided by external data sets summarized in section 2.4. The model was run once with each emission option, each time for the same 13 months (June 2006 to June 2007), preceded by a 3-month spin-up, with all other settings (e.g., anthropogenic and natural emissions) kept the same. Daily BB emissions were prepared off-line and then read into the model. BB emissions at injection were evenly distributed within the GEOS-4 defined boundary layer, according to the standard GOCART procedure.

[32] Aerosol optical depth is determined from the dry mass concentrations and mass extinction coefficients for the major aerosol types, which are functions of aerosol size distributions, refractive indices, and humidity-dependent hygroscopic growth. Total AOD is the sum of optical depths of individual aerosol types: dust, black carbon, particulate organic matter, sulfate, and sea salt. The AOD calculation methods, as well as the sources and values of the relevant parameters, are described by Chin *et al.* [2002, 2009].

3.2. Satellite Observations of Aerosol

3.2.1. MODIS Aerosol Optical Depth

[33] MODERate resolution Imaging Spectroradiometer (MODIS) is a key instrument on board NASA’s Terra and Aqua satellites. With a wide 2330 km swath, MODIS observes the whole globe in 1 to 2 days with more frequent coverage at higher latitudes. Measurements made in 36 spectral bands between 0.405 and $14.385 \mu\text{m}$ are the source for a number of land, ocean and atmospheric products with band-dependent nominal spatial resolutions of 250 m, 500 m, or 1 km (<http://modis.gsfc.nasa.gov/about/>). We use here the 550 nm AOD from the MODIS Collection 5 level II aerosol product (MOD04 or MYD04 from the MODIS instruments on Terra and Aqua satellites, respectively) at 10 km resolution [Levy *et al.*, 2010; Remer *et al.*, 2006]. For each BB event, only one MODIS snapshot is used, from MOD04 or MYD04, as appropriate. All 10-km pixels where AOD retrievals are available are averaged to the $1^\circ\text{lat} \times 1.25^\circ\text{lon}$ GOCART grid for further comparison with the model AOD.

3.2.2. MISR Stereo Height and Aerosol Products

[34] The Multiangle Imaging SpectroRadiometer (MISR) on board NASA’s Terra satellite has a unique geometry, where it is looking down on Earth with nine cameras, precisely aligned to sequentially view a 380 km-wide swath at nine different angles in four spectral bands (blue, green, red, and near-infrared), providing global coverage every 9 days [Diner *et al.*, 1998]. To evaluate the height of smoke layers we use the MISR operational level 2 stereo height product (from <http://eosweb.larc.nasa.gov/>), which reports cloud and near-source aerosol plume heights globally, on a 1.1-km grid, and with vertical accuracy of about 0.5 km [Moroney *et al.*, 2002]. The MISR aerosol product includes AOD and aerosol type constraints globally [Kahn *et al.*, 2010], and is used here in some cases to confirm plume locations when assessing their height.

3.2.3. CALIPSO Vertical Feature Mask

[35] The CALIPSO satellite carrying the CALIOP (Cloud-Aerosol Lidar with Orthogonal Polarization) lidar system is a part of the ‘A-train’ constellation of sun-synchronous

Table 3. Emission Estimates Used as Input to the GOCART Model

	Mod1-CCI- GOCART	Mod1-CCm- GOCART	Mod1-GLC- GOCART	Mod1- GLC-GLC	MCD45-CCI- GOCART	MCD45-CCm- GOCART	MCD45-GLC- GOCART	MCD45- GLC-GLC	GFED3d- GOCART	GFED3m- GOCART	GFED2m- GOCART	QFED
Based on MODIS active fire counts (mod1)	X	X	X	X								
MODIS collection 5 burned area product-MCD45A1 (MCD45)					X	X	X	X				
Carbon consumption (CC) data set, converted to effective fuel load using Haines index (CCI)	X											
CC data set, converted to effective fuel load assuming all fires of medium severity (CCm)		X										
GLC2000 effective fuel load (GLC)			X	X			X	X				
GFED version 3-daily dry mass burned (GFED3d)								X	X			
GFED version 3-monthly dry mass burned (GFED3m)										X		
GFED version 2-monthly dry mass burned (GFED2m)											X	
QFED2-daily BC, OC and SO ₂ emissions (QFED)												X
Standard GOCART F_j (GOCART)	X	X	X	X			X	X				
GLC2000 emission factors (GLC)					X			X				
GFED version 3 emission factors									X			X

Burned Area Products

Fuel Consumption, Dry Mass, and Emission Products

Emission Factor Options

satellites, which cross the equator in the early afternoon around 1:30 P.M. local time in an ascending orbit. The CALIPSO vertical feature mask provides vertical and horizontal distributions of cloud and aerosol layers with 5 km spatial resolution [Vaughan *et al.*, 2004; Winker *et al.*, 2009]. Aerosol and cloud layers are classified by associating measured optical or physical parameters (such as attenuated backscatter coefficient, or color ratio) with particular classes of known atmospheric scatterers. The Vertical Feature Mask is used here to evaluate smoke height in the studied cases, where CALIPSO observations are available. Daily CALIOP data are available at http://eosweb.larc.nasa.gov/PRODOCS/calipso/table_calipso.html.

3.3. Biomass Burning Events

[36] One hundred and twenty four fire events, occurring between June 2006 and June 2007 in different regions of the world, were used to evaluate the emission options. These events include a range of fire sizes, seasons, types of vegetation, and burning conditions. Fire cases were selected to include smoke plumes, which are defined as smoke-like features appearing in MODIS visible images, supported by the presence of fire pixels reported in MODIS thermal anomalies product (MOD14/MYD14 for Terra and Aqua MODIS respectively), and at the same time showing elevated AOD in the MODIS AOD data. Thus, the sizes of study cases vary considerably, and can include single fires with associated smoke plumes, such as several events in the U.S., areas of generally hazy regions containing many fires with or without individual visible plumes, such as the agricultural burning in Africa, Eastern Europe or South America, and cases where large individual smoke plumes merge to produce thick smoke clouds, such as several cases in Russia, Canada, Indonesia, and South Australia. Table 4 provides a list of fire cases studied; it gives their unique identification numbers, specifies their geographic boundaries defined by latitude and longitude corners, reports the date of MODIS observation, and denotes the MODIS-carrying satellite used by letters “A” or “T,” which stand for Aqua and Terra, respectively.

[37] To locate the fire events, we used as a starting point events featured on the Earth Observatory web site, which provides a selection of fires in the Natural Hazards/Fires category (<http://earthobservatory.nasa.gov/NaturalHazards>). We also used a combination of MODIS visible browse images (<http://modis-atmos.gsfc.nasa.gov/IMAGES/>) and the locations of fire detections from the MOD14A1 and MYD14A1 thermal anomalies products to identify the locations and times of burning events. A subset of these events was chosen for analysis, based on whether smoke or general haziness, un-obscured by condensate cloud, appears in visible images of the region. Figure 1 displays a map showing the locations of the cases studied. They are grouped into geographic regions having roughly similar burning conditions.

[38] In selecting the fire cases, we also considered biomass burning seasons in different regions. These seasons are described elsewhere [Dey and Di Girolamo, 2010; Duncan *et al.*, 2003; Giglio, 2010; Giglio *et al.*, 2006a] and are mentioned in Table 4. Table 4 also provides a description of prevailing vegetation and characteristics of burning in each world region.

[39] In regions with strong dust sources, such as northern India and North Africa, we consider the seasonality of dust

emissions as those times when dust significantly contributes to the total AOD. Much of the spring peak of forest and harvest burning in India coincides with the pre-monsoon dust season [Dey and Di Girolamo, 2010], so most burning cases are selected during early spring or during the smaller burning season in November. Similarly, major biomass burning in sub-equatorial Africa during boreal winter coincides with the November–March season of dust transport [Pandithurai *et al.*, 2001], and therefore fire cases were chosen at the onset of the burning season - in November to minimize the dust influence.

[40] Years 2006 and 2007 were those of very little biomass burning in Alaska, so only few cases were observed by MODIS, out of which only four were both large enough to be seen from space and sufficiently un-obscured by clouds to be used for this analysis.

4. Results and Discussion

4.1. Comparison of Emission Options

[41] The emission options defined in section 2.4 provide a range of BB emission estimates. Figure 2a shows total dry mass burned globally in 2006, as estimated by each emission option. Instead of comparing emission estimates for the June 2006–June 2007 study period, we compared estimates for full years of 2006 (shown in Figure 2) and 2007 (not shown here) so that our results could be compared to previous studies [e.g., van der Werf *et al.*, 2010]. Since the QFED inventory calculates aerosol emissions directly from MODIS-measured FRP, it does not provide a DM estimate. Figure 2b illustrates the differences in corresponding 2006 global BB emissions of BC. The comparisons for OC and SO₂ (not shown here) produce patterns similar to those of BC. The magnitudes of SO₂ emissions are similar to those of BC, and OC emissions are approximately eight times larger, as expected from the values of species emission factors introduced in section 2.1.3. Comparisons of both DM and emissions of individual aerosol species for 2007 also show similar patterns.

[42] The differences between individual emission options can be quite large. Thus, the largest estimate of global total BC emissions by the mod1-CCm-GOCART option is about eight times larger than that of GFED3. These differences can be explained by the choice of parameters that were combined according to equation (1). Some of these differences are briefly discussed below.

[43] Estimates of burned area by MCD45, GFED3, and a version of mod1 were compared in detail in previous studies by Roy *et al.* [2008] and Giglio *et al.* [2010]. Although the total burned areas reported by all three products globally in 2006 are very similar: 3.94×10^6 km² in mod1, 3.96×10^6 km² in MCD45, 3.41×10^6 km² in GFED3, their performance in different ecosystems is noticeably distinct. Roy *et al.* [2008] demonstrated that in ecosystems having low Leaf Area Index (LAI) and low percent tree cover—shrublands, grasslands, and savannas, the active fire product (mod1) estimates less burned area (BA) than MCD45. On the other hand, when the percent tree cover is high, especially in evergreen forests (both needleleaf (mostly in boreal regions) and broadleaf (mostly in equatorial regions)), mod1 reports more BA compared to MCD45. GFED3 burned area estimates are similar to those from MCD45 in many regions [Giglio *et al.*, 2010]. Croplands are an exception to this pattern, and although having low LAI

Table 4. Study Cases by Region With the Regional Specifics of Biomass Burning

Region and Biomass Burning Season(s)	Case Number, T/A, Date (yyyy-mm-dd), and Coordinates [SW Corner; NE Corner]	AOD Threshold in Figure 5	AOD Symbol in Figure 5	Dominant Vegetation Type(s); Characteristics of Burning; Some Notes on MODIS AOD	
Alaska, Jun–Aug	42 T (2006-06-04) [60N 165W; 64N 160W]	0.15	diamond	Tree cover: mosaic with other natural vegetation, evergreen; evergreen shrubs. Individual fires with associated smoke plumes. MODIS AOD is not usually retrieved in plume cores.	
	43 T (2006-06-05) [58N 165W; 64N 155W]	0.15	triangle		
	46 T (2006-07-23) [62N 145W; 64N 135W]	0.05	square		
Canada, Jun–Sep	122 T (2006-06-15) [67N 147W; 69N 139W]	0.15	circle	Tree cover: needleleaved, mixed leaf type, mosaic with other natural vegetation. Individual fires with associated smoke plumes combine into large-scale plumes/smoke regions. MODIS AOD is often not retrieved in plume cores.	
	1 T (2006-07-04) [50N 130W; 65N 100W]	0.15	diamond		
	2 T (2006-06-26) [48N 110W; 60N 95W]	0.15	triangle		
China, Jan–Apr, Aug–Oct	3 T (2006-06-27) [40N 116W; 64N 85W]	0.15	square	Mosaic: Cropland, tree cover, other natural vegetation; Tree cover: needleleaved, broadleaved. Many fires with no distinct smoke plumes create overall hazy/smoky area.	
	31 T (2007-05-10) [47N 92W; 51N 87W]	0.1	circle		
	70 A (2006-08-31) [49N 100W; 62N 80W]	0.15	inverted triangle		
	74 A (2006-09-06) [52N 97W; 55N 88W]	0.1	right-facing triangle		
	113 T (2006-07-05) [48N 110W; 60N 90W]	0.15	left-facing triangle		
	114 T (2006-09-10) [53N 113W; 65N 90W]	0.15	hourglass		
	37 T (2007-05-29) [29N 108E; 37N 122E]	0.4	diamond		
	55 T (2006-08-15) [24N 116E; 36N 124E]	0.4	triangle		
	59 T (2006-09-22) [24N 104E; 40N 126E]	0.4	square		
	60 T (2006-10-05) [26N 110E; 44N 125E]	0.4	circle		
61 T (2006-10-30) [22N 110E; 42N 124E]	0.4	inverted triangle			
Europe, Mar–May, Jun–Oct	94 A (2007-04-29) [38N 124E; 41N 130E]	0.15	right-facing triangle	Cultivated and managed areas; Mosaic: Cropland, tree cover, other natural vegetation. Fires with or without detectable associated smoke plumes create overall hazy/smoky area.	
	51 T (2006-07-28) [40N 16E; 48N 30E]	0.2	diamond		
	53 T (2006-08-02) [44N 27E; 50N 40E]	0.2	triangle		
	54 T (2006-08-04) [44N 30E; 54N 47E]	0.2	square		
	69 T (2006-09-01) [52N 54E; 60N 66E]	0.15	circle		
	85 T (2006-08-07) [38N 13W; 43N 8W]	0.15	inverted triangle		
	86 T (2006-08-09) [40N 13W; 43N 8W]	0.15	right-facing triangle		
	87 A (2006-08-13) [39N 11W; 43N 7W]	0.15	left-facing triangle		
	132 A (2006-08-03) [44N 37E; 50N 44E]	0.15	hourglass		
	133 T (2006-08-06) [42N 37E; 46N 47E]	0.1	sideways hourglass		
	17 T (2006-11-05) [22N 70E; 35N 92E]	0.1	diamond		Cultivated and managed areas. Fires with or without detectable associated smoke plumes create overall hazy/smoky area.
	41 A (2006-10-15) [28N 72E; 33N 80E]	0.1	triangle		
	123 A (2007-03-26) [16N 78E; 21N 82E]	0.15	square		
124 A (2007-03-01) [12N 78E; 17N 80E]	0.15	circle			
125 A (2007-03-06) [18N 81E; 22N 86E]	0.15	inverted triangle			
126 A (2007-03-08) [16N 78E; 20N 83E]	0.2	right-facing triangle			
127 A (2007-03-17) [17N 78E; 22N 86E]	0.15	left-facing triangle			
128 A (2007-05-02) [29N 71E; 33N 77E]	0.2	hourglass			
129 A (2007-05-07) [29N 70E; 34N 78E]	0.2	sideways hourglass			
13 T (2006-10-12) [6S 104E; 2N 120E]	0.2	diamond	Tree cover: broadleaved; cropland/shrubs and /or grass. Individual fires with associated smoke plumes combine into large-scale plumes/smoke regions. MODIS AOD is often not retrieved in plume cores.		
14 T (2006-10-05) [6S 104E; 2N 120E]	0.1	triangle			
15 T (2006-10-04) [8S 100E; 4N 108E]	0.15	square			
16 T (2006-09-27) [6S 100E; 1N 108E]	0.15	circle			
135 A (2006-10-02) [6S 100E; 2N 106E]	0.15	inverted triangle			
136 A (2006-10-11) [6S 101E; 3N 106E]	0.15	right-facing triangle			

Table 4. (continued)

Region and Biomass Burning Season(s)	Case Number, T/A, Date (yyyy-mm-dd), and Coordinates [SW Corner; NE Corner]	AOD Threshold in Figure 5	AOD Symbol in Figure 5	Dominant Vegetation Type(s); Characteristics of Burning; Some Notes on MODIS AOD	
L-America, Mar–Jun	32 A (2007-05-12) [12N 88W; 16N 83W]	0.15	diamond	Tree cover: broadleaved; cropland/shrubs and /or grass. Fires with or without detectable associated smoke plumes create overall hazy/smoky area.	
	33 A (2007-05-13) [12N 88W; 16N 83W]	0.15	triangle		
	35 A (2007-04-11) [15N 93W; 18N 89W]	0.15	square		
	36 T (2007-04-11) [15N 93W; 19N 88W]	0.1	circle		
	107 T (2007-05-02) [15N 94W; 21N 90W]	0.1	inverted triangle		
	108 T (2007-05-11) [15N 92W; 21N 89W]	0.15	right-facing triangle		
	110 A (2007-04-18) [15N 92W; 19N 88W]	0.15	left-facing triangle		
	112 A (2007-05-22) [16N 97W; 20N 90W]	0.15	hourglass		
	57 T (2006-09-16) [18S 122E; 15S 130E]	0.1	diamond		Shrub cover; herbaceous cover. Individual fires, some with weak associated smoke plumes. MODIS AOD is often not retrieved with intermittent clouds and bright surface.
	58 T (2006-09-18) [20S 122E; 12S 134E]	0.1	triangle		
	65 A (2006-11-22) [28S 146E; 23S 154E]	0.1	square		
	66 A (2006-11-22) [22S 134E; 15S 146E]	0.1	circle		
67 A (2006-11-22) [26S 114E; 16S 128E]	0.15	inverted triangle			
68 T (2006-11-24) [20S 130E; 12S 146E]	0.1	right-facing triangle			
103 A (2007-06-10) [15S 130E; 12S 135E]	0.15	left-facing triangle			
104 A (2006-11-17) [27S 146E; 24S 154E]	0.1	hourglass			
105 A (2006-11-20) [16S 141E; 12S 144E]	0.15	sideways hourglass			
106 A (2006-10-04) [12S 130E; 10S 132E]	0.1	vertical rectangle			
21 A (2007-01-05) [2N 12E; 9N 22E]	0.15	diamond	Tree cover: broadleaved, mixed; shrubs; cropland. Many fires with no distinct smoke plumes create overall hazy/smoky area		
62 T (2006-11-16) [4N 22E; 12N 34E]	0.15	triangle			
63 T (2006-11-16) [7N 15W; 16N 5W]	0.15	square			
64 T (2006-11-18) [4N 12E; 12N 23E]	0.1	circle			
118 A (2006-11-26) [8N 6W; 10N 5E]	0.15	inverted triangle			
119 A (2006-11-23) [8N 5W; 12N 4E]	0.15	right-facing triangle			
120 A (2006-12-03) [8N 14W; 14N 9W]	0.1	left-facing triangle			
10 T (2006-07-17) [56N 85E; 66N 115E]	0.15	diamond		Tree cover: needleleaved, mixed leaf type, mosaic with other natural vegetation. Individual fires with associated smoke plumes combine into large-scale plumes/smoke regions. MODIS AOD is often not retrieved in plume cores.	
11 T (2006-07-20) [50N 80E; 70N 110E]	0.15	triangle			
47 T (2006-07-25) [60N 75E; 80N 130E]	0.15	square			
48 T (2006-07-25) [56N 70E; 80N 145E]	0.15	circle			
50 T (2006-07-27) [51N 103E; 75N 137E]	0.15	inverted triangle			
102 A (2006-07-24) [57N 82E; 68N 114E]	0.15	right-facing triangle			
38 A (2006-08-21) [18S 70W; 6S 56W]	0.15	diamond	Tree cover: broadleaved evergreen, deciduous; cropland/shrubs and /or grass. Individual fires with or without associated smoke plumes, generally hazy, but some combine into larger plumes. MODIS AOD is often not retrieved in complex cloudy scenes.		
39 T (2006-08-21) [20S 70W; 4S 58W]	0.15	triangle			
40 A (2006-08-24) [22S 73W; 5S 58W]	0.15	square			
44 A (2006-07-07) [32S 64W; 22S 54W]	0.1	circle			
45 T (2006-07-12) [20S 62W; 10S 54W]	0.1	inverted triangle			
56 T (2006-08-31) [23S 64W; 4S 52W]	0.15	right-facing triangle			
89 A (2007-01-13) [38S 75W; 33S 72W]	0.1	left-facing triangle			
18 T (2006-12-04) [39S 142E; 33S 150E]	0.1	diamond		Three cover: broadleaved evergreen; cropland. Individual fires with associated smoke plumes combine into large-scale plumes/smoke regions, or Fires with or without detectable associated smoke plumes create overall hazy/smoky area.	
19 T (2006-12-18) [40S 144E; 32S 156E]	0.1	triangle			
20 T (2006-12-20) [40S 144E; 36S 150E]	0.1	square			
96 T (2007-01-10) [39S 145E; 37S 150E]	0.15	circle			
97 T (2006-12-05) [41S 145E; 35S 151E]	0.15	inverted triangle			
NAustralia, Aug–Nov					
Russia, Apr–Oct					
	SAustralia, Feb–May				

Table 4. (continued)

Region and Biomass Burning Season(s)	Case Number, T/A, Date (yyyy-mm-dd), and Coordinates [SW Corner; NE Corner]	AOD Threshold in Figure 5	AOD Symbol in Figure 5	Dominant Vegetation Type(s); Characteristics of Burning; Some Notes on MODIS AOD		
SCAfrica, Jun–Oct	100 A (2006-04-13) [39S 147E; 35S 150E]	0.1	right-facing triangle	Tree cover: broadleaved. Many fires with no distinct smoke plumes create overall hazy/smoky area		
	101 A (2006-04-20) [40S 147E; 35S 150E]	0.1	left-facing triangle			
	134 A (2006-12-08) [39S 143E; 34S 153E]	0.1	hourglass			
		12 T (2006-06-24) [16S 6E; 0 26E]	0.15	diamond		
		49 A (2006-07-26) [18S 12E; 5S 32E]	0.15	triangle		
		115 A (2007-06-24) [13S 19E; 5S 28E]	0.15	square		
		116 A (2007-06-13) [13S 22E; 8S 30E]	0.1	circle		
		117 A (2006-08-04) [23S 32E; 16S 37E]	0.1	inverted triangle		
		121 A (2007-05-28) [12S 14E; 4S 24E]	0.1	right-facing triangle		
	SEAsia, Jan–Jun, Sep–Nov	25 A (2007-03-04) [16N 97E; 24N 108E]	0.15	diamond	Cropland; tree cover: needleleaved, broadleaved; shrub cover. Fires with or without detectable associated smoke plumes create overall hazy/smoky area.	
		27 T (2007-01-26) [11N 100E; 16N 108E]	0.15	triangle		
		28 A (2007-01-28) [11N 100E; 16N 108E]	0.15	square		
90 A (2007-04-02) [18N 98E; 24N 106E]		0.15	circle			
91 A (2007-03-13) [16N 97E; 23N 105E]		0.15	inverted triangle			
92 A (2007-03-18) [13N 96E; 24N 102E]		0.15	right-facing triangle			
93 A (2007-03-27) [20N 93E; 26N 95E]		0.15	left-facing triangle			
95 A (2007-03-02) [18N 93E; 23N 96E]		0.15	hourglass			
EUSA, Feb–Jun		23 A (2007-03-07) [30N 91W; 34N 82W]	0.1	diamond		Cropland; tree cover: needleleaved, broadleaved; shrub cover. Fires with or without detectable associated smoke plumes create overall hazy/smoky area.
		24 T (2007-03-07) [30N 96W; 36N 88W]	0.1	triangle		
	75 T (2007-03-20) [30N 88W; 35N 80W]	0.15	square			
	76 T (2007-05-20) [30N 84W; 34N 81W]	0.15	circle			
	109 A (2007-05-12) [26N 85W; 33N 81W]	0.15	inverted triangle			
	111 T (2007-05-22) [1N 86W; 35N 81W]	0.15	right-facing triangle			
	WUSA, Jun–Nov	4 T (2006-07-16) [44N 110W; 48N 104W]	0.1	diamond	Three cover: needleleaved; shrub cover. Individual fires with associated smoke plumes. Heterogeneous terrain and vegetation leads to many omissions in AOD retrievals and fire detections and characterization. MODIS AOD is often not retrieved in plume cores.	
		5 T (2006-07-18) [45N 110W; 50N 104W]	0.1	triangle		
		7 T (2006-09-12) [42N 118W; 50N 105W]	0.1	square		
		8 T (2006-06-20) [34N 107W; 41N 102W]	0.1	circle		
		9 T (2006-12-03) [32N 122W; 36N 117W]	0.1	inverted triangle		
71 A (2006-10-26) [32N 120W; 35N 116W]		0.15	right-facing triangle			
72 A (2006-08-16) [41N 117W; 44N 110W]		0.15	left-facing triangle			
73 A (2006-09-06) [44N 124W; 54N 110W]		0.15	hourglass			
77 A (2006-07-25) [46N 122W; 49N 116W]		0.1	sideways hourglass			
78 A (2006-08-02) [48N 122W; 50N 117W]		0.15	vertical rectangle			
79 A (2006-08-02) [38N 125W; 43N 120W]		0.15	horizontal rectangle			
80 T (2006-08-07) [48N 121W; 54N 113W]		0.15	top half circle			
81 T (2006-08-20) [47N 122W; 52N 113W]		0.15	bottom half circle			
82 A (2006-08-27) [47N 124W; 52N 117W]		0.15	right half circle			
83 A (2006-08-28) [48N 122W; 51N 115W]		0.15	left half circle			
84 A (2006-08-28) [44N 118W; 48N 112W]		0.15	cross			

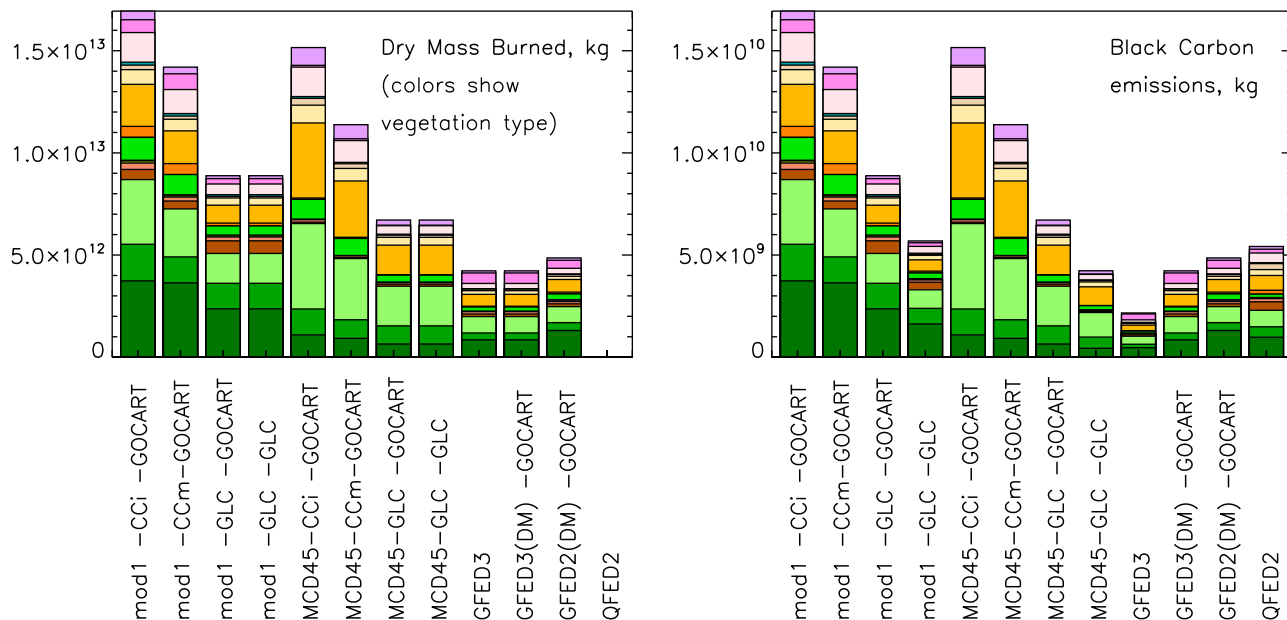


Figure 2. (left) Total dry mass (DM) burned globally in 2006, reported by GOCART emission input options considered in this study. Since DM is a product of burned area and effective fuel load and does not take into account emission factors, DM estimates for emission options like mod1-GLC-GOCART and mod1-GLC-GLC are the same. (right) Total global emission of BC, each column representing one emission option. Colors in each bar correspond to dry mass burned (left) or BC emissions (right) from the GLC vegetation categories outlined in Figure 1.

at the time of burning, more BA is reported globally by mod1 than the MCD45 algorithm for this category [Roy *et al.*, 2008], with GFED3 BA being even lower than MCD45 in croplands [Giglio *et al.*, 2010].

[44] Since most of the area burned is a result of fires in Africa, followed by South America and Australia, BB emissions from vegetation types dominant in these regions (GLC codes 1, 3, and 12) show the largest absolute differences, consistent with the described BA detection patterns. The differences in estimated BA and subsequent emissions can be quite large regionally, such as in boreal regions covered by evergreen needleleaf forests (GLC code 4), or in tropical crops and shrubs (GLC code 17), but their contribution to total global emissions is relatively small.

[45] The effective fuel load ($B^*\beta$ in equation (1)) products chosen have not been explicitly compared elsewhere. Effective fuel load estimates provided by the WEB-FE CC data set for low (CCi), medium (CCm) and high (CCh) fire severity are mapped in Figures 3a–3c. The CCi estimate is computed using all three CC estimates and Haines Index as described in section 2.1.2 above. The map of GLC effective fuel load estimates is given in Figure 3d. CC and GLC provide gridded estimates of effective fuel load values, which are essentially assumed to be constant. However, since no static effective fuel load is provided in the GFED3 data set, we obtained the equivalent effective fuel load by dividing the GFED3 monthly values of burned dry mass by the corresponding value of burned area in every GOCART grid box. Average effective fuel load from all the available data for the period of 1997–2009 is shown in Figure 3e. The maps of absolute effective fuel load differences emphasize the discrepancies between the data sets, where the largest differences are in the forested boreal and tropical regions. CC estimates of

effective fuel load by fires of high severity (CCh) have the largest values, and CCi - the lowest. Assuming all fires of medium fire severity for a reference, we compare the absolute values of effective fuel load in the data sets. The general trend, which shows the CCm data set including all fires of medium severity (CCm) as giving the largest effective fuel load estimates, followed by the GLC and GFED3, is reversed in the boreal needleleaf forest, where the GFED3 effective fuel load is the largest, followed by GLC and CCm, and is partially reversed in the parts of tropical forest where GFED3 is the largest, followed by CCm and GLC.

[46] The Haines Index tends to increase the average daily effective fuel load in most regions if it serves as a proxy for fire severity to determine effective fuel load, as described in section 2.1.2.

[47] As can be seen from the global average values given in Table 1, the GLC and GFED emission factors are similar and are all generally lower than the GOCART standard F_j 's. Regionally, this difference is smallest in the extra-tropical forest, and is largest in the grasslands and shrublands, where the standard GOCART option can be up to a factor 2 to 3 larger than either the GLC or GFED F_j 's. Because, as has been mentioned earlier, grassland and savanna burning in Africa, Australia and South America are the greatest contributors to BB emissions globally, such a significant difference in emission factors for these vegetation categories magnifies the differences in estimated emissions when accumulated over vast burned areas and long burning seasons. Also, as will be discussed below in section 4.4, small deviations in estimated emission rates are likely to have noticeable effects on the simulated AOD, so further study of the appropriate emission factors in the African and South American ecosystems is needed.

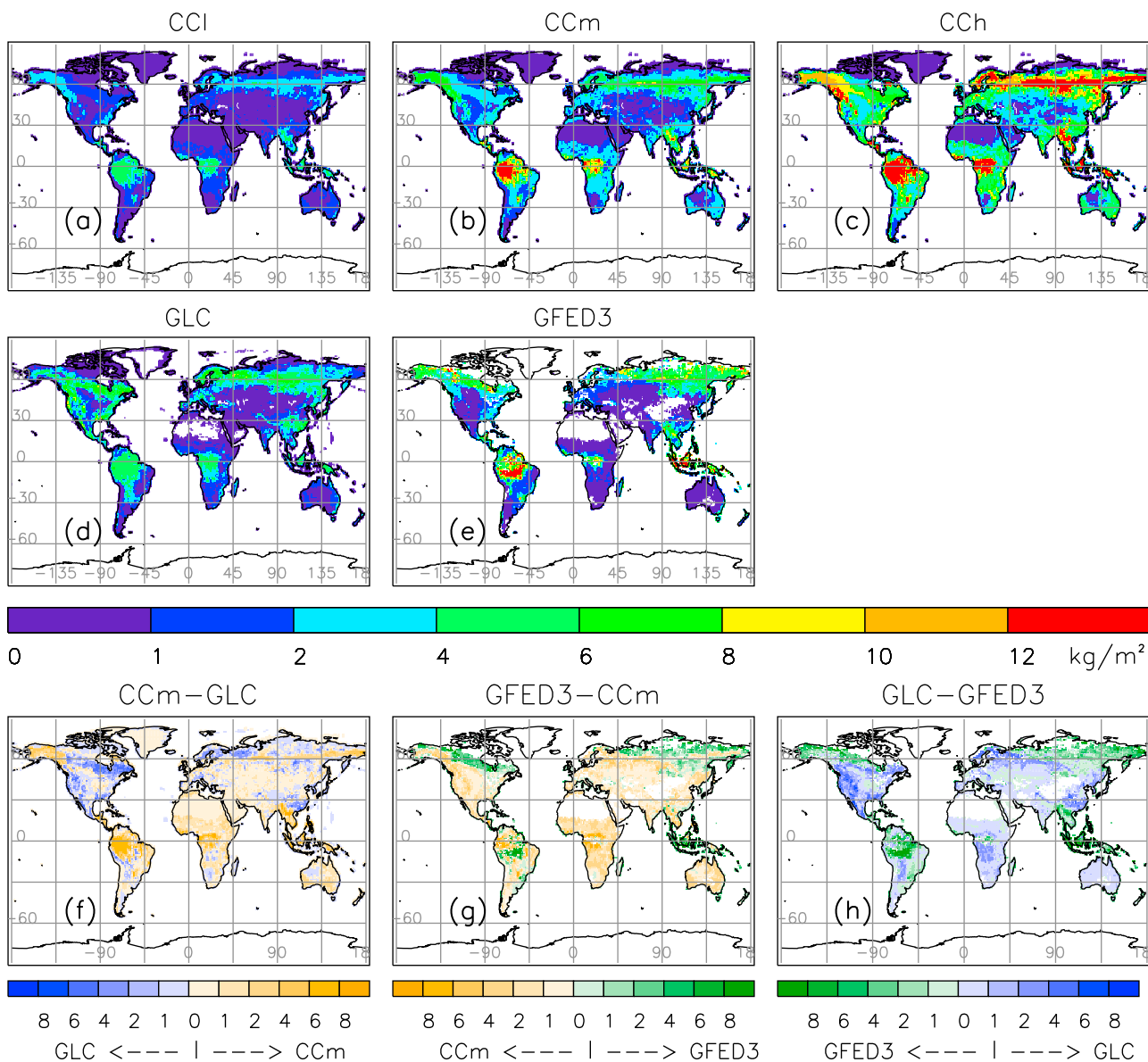


Figure 3. Effective fuel load estimates in kg/m^2 , by the Carbon Consumption (CC) inventory for (a) low, (b) medium, and (c) high fire severity; (d) GLC; and (e) GFED3 data sets. Absolute differences between (f) CCm, (g) GFED3, and (h) GLC fuel load are shown.

4.2. Evaluation of Emission Options Using GOCART and MODIS AOD

[48] We compared GOCART AOD, sampled at the closest time to the satellite overpass from each of the 13 model runs, with MODIS AOD averaged to the model grid. The maps of MODIS and GOCART AOD within each case box were visually inspected to evaluate the spatial features of the simulated plume. As an example, Figure 4 shows the MODIS visible image, retrieved MODIS AOD with original 10-km resolution, re-gridded MODIS AOD to model grid, and snapshots of GOCART AOD from all runs with different emission options for case 11 in Russia on July 20, 2006. As noted earlier, the QFED data set uses MODIS AOD as one of the input data sets for estimating emissions, so AOD from QFED-based GOCART runs cannot be fairly compared to MODIS AOD.

[49] To limit analysis of aerosol properties to smoke within the plumes, a threshold AOD value (provided in Table 4) was chosen by visual inspection of MODIS and GOCART AOD maps for each case, with the aim of separating the smoke plumes from background. The values of all pixels where AOD exceeded the threshold were considered in calculating average AOD values for MODIS observations and model simulations in each case.

[50] Since BB aerosol emissions consists mainly of BC and OC [Andreae and Merlet, 2001; Seinfeld and Pandis, 1998], BB emissions are represented by the sum of BC and OC emissions in subsequent analysis. The GOCART model works with aerosol emissions in terms of emission rates, expressed in units of mass of aerosol species per unit area per unit time. Therefore, to use satellite AOD as a

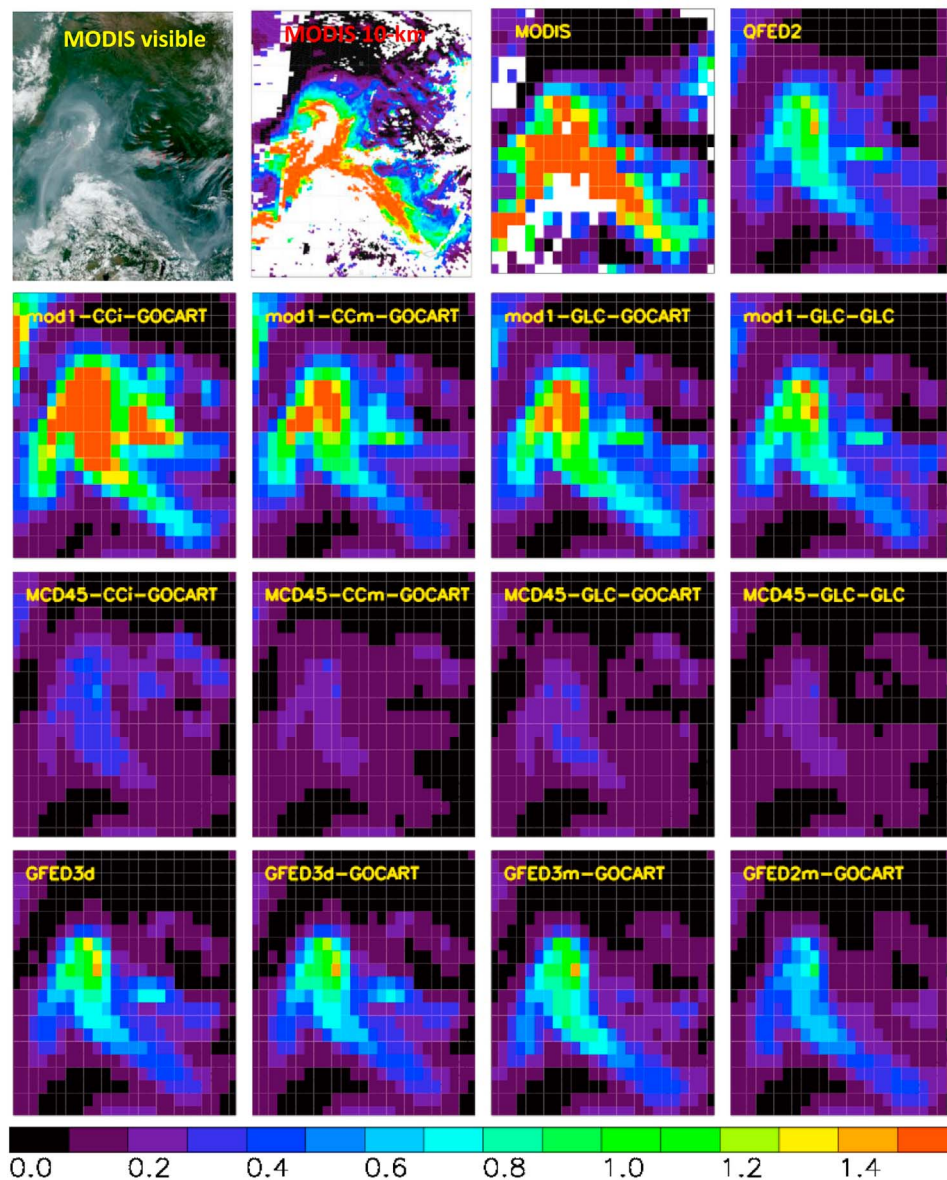


Figure 4. Case 11: Russia, 20 July 2006. Terra-MODIS visible image of the scene with fire locations marked in red; total column MODIS AOD with original 10-km resolution, as provided by MOD04 data product; and MODIS total TOA AOD averaged to GOCART grid, followed by maps of the temporally closest 3-h output of instantaneous GOCART AOD values for different emission options. Emission options used as input to each of the model runs are labeled on top of the corresponding maps.

constraint for BB emissions in the model, we first explore the relationship between emissions input into the model and simulated AOD output. This relationship is plotted in Figure 5. To keep the analysis independent of the fire case box size, we use units of emission rate ($\text{kgC km}^{-2} \text{day}^{-1}$) to characterize emission amount. The values from all model runs and all fire cases are colored according to the region where the fire is located. The region colors are defined in Figure 1.

[51] The same data set, plotted for each region separately, follows in Figure 6. Colors are used here to represent different emission options, and symbols distinguish different fire cases occurring within a given region. Symbols corresponding to each fire case are given in Table 4. The

symbol associated with the emission option that produces the average GOCART AOD closest to the average MODIS AOD for each case is highlighted in black. Connected to each such symbol is a black line showing the difference between this model average AOD and the MODIS average AOD for this case (i.e., the MODIS AOD measurement would plot at the end of this black line). We introduce the black GOCART AOD symbol closest to the MODIS AOD to place the MODIS AOD reference on the plot, but in the absence of the true aerosol emission rate, we resort to looking for the closest model estimate.

[52] When the average AOD for each case is plotted against the corresponding BB aerosol emission rate, the data points in Figures 5 and 6 form a pattern of two distinct regimes.

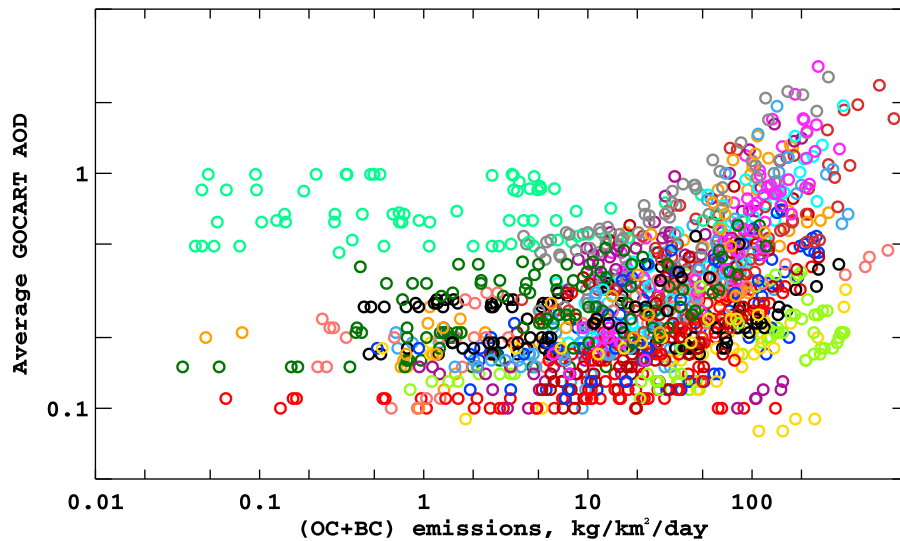


Figure 5. Average GOCART AOD for each fire case and each model run plotted against average emission rate for the corresponding case in the corresponding emission option. Data points are colored by geographic region, with colors defined in Figure 1.

[53] 1. In the first regime the points are clustered parallel to the horizontal axis. These are regions dominated by background aerosol, where the BB contribution does not significantly affect the total AOD. This happens, for example, when the BB AOD is very low and is not much higher than AOD of the environment, such as in some cases in the USA. Alternatively, the background aerosol loading can be so high that even substantial BB emissions do not contribute a dominant fraction to the total AOD. Such are the cases in China and India. Qualitatively, in the areas where AOD is dominated by non-BB aerosols, different BB inventories make little differences in GOCART AOD. In contrast, even though the non-BB background AOD is also rather high in South-East Asia, North-Central Africa, and Central and Eastern Europe, the contribution of BB aerosol is significant enough that the choice of emission inventory measurably affects the total AOD. The contribution to total AOD in the model from different aerosol types was evaluated both spatially and in magnitude to come to this conclusion. Wind dispersal, which also tends to flatten the curves in Figure 6 regardless of background aerosol level, is discussed in Section 4.3 below.

[54] 2. In the second regime, AOD depends on the amount of smoke emissions. This “BB-dominated” regime appears after a certain amount of emissions has been reached, i.e., after the contribution of BB aerosol to total AOD starts to noticeably outweigh the background aerosol components.

[55] The spread of the data points along the x axis in each case in Figure 6 (cases are distinguished by different symbols here) shows the range of estimates provided by different emission options. The spread of values is generally larger, i.e., the discrepancies between emission rates estimated by different inventories are large, in background-dominated areas where the area is polluted (India, China, Eastern Europe), where the observed plume is not well-defined or small (some U.S. cases, Alaska), or where the event is long-lasting, so overlying thick smoke prevents good observations of burned area and fire properties (some cases in Canada,

Indonesia). In BB emission-dominated regions (Russia, North Australia, South America), emission estimates from different emission options are fairly similar, but given a steep slope of the AOD versus (BC + OC) emissions relationship, even a small change in emission amount has a significant effect on the simulated AOD.

[56] The regional performance of the model with different emission inventories is further presented in a series of maps and scatterplots in Figures 7 and 8. Each panel in these figures shows the performance of GOCART with BB aerosol estimated by one of the emission options. The color of each case box in Figure 7 shows the ratio of average GOCART AOD to average MODIS AOD. The darker the red color, the more GOCART overestimates AOD relative to MODIS, and the darker the blue color, the lower the GOCART AOD compared to MODIS. Green color marks the cases where GOCART average AOD is within about 20% of MODIS average AOD. The scatterplots in Figure 8 compare MODIS and GOCART average AOD for each fire case studied. The data points are colored by region where the fire cases are located (see Figure 1). The clusters of data from the same region relative to the 1:1 line also show the performance of the GOCART model using a given emission option in this region.

[57] The overall performance of each emission option in all regions is generalized by the statistics describing the comparison of GOCART and MODIS average AOD values: correlation coefficient R , which reveals linear correspondence between the data sets, mean bias B representing the ratio of the model results to data, and root mean square error RMSE, which shows the magnitude of absolute difference between the model and the observations [Chin *et al.*, 2004]. These statistics are shown in each panel of Figure 8 and are also given in Table 5. Higher R combined with lower RMSE and B close to unity indicate that the average GOCART AOD with the given BB emission option compares better with the average MODIS AOD.

[58] Regarding the regional performance of individual emission options, we find the following.

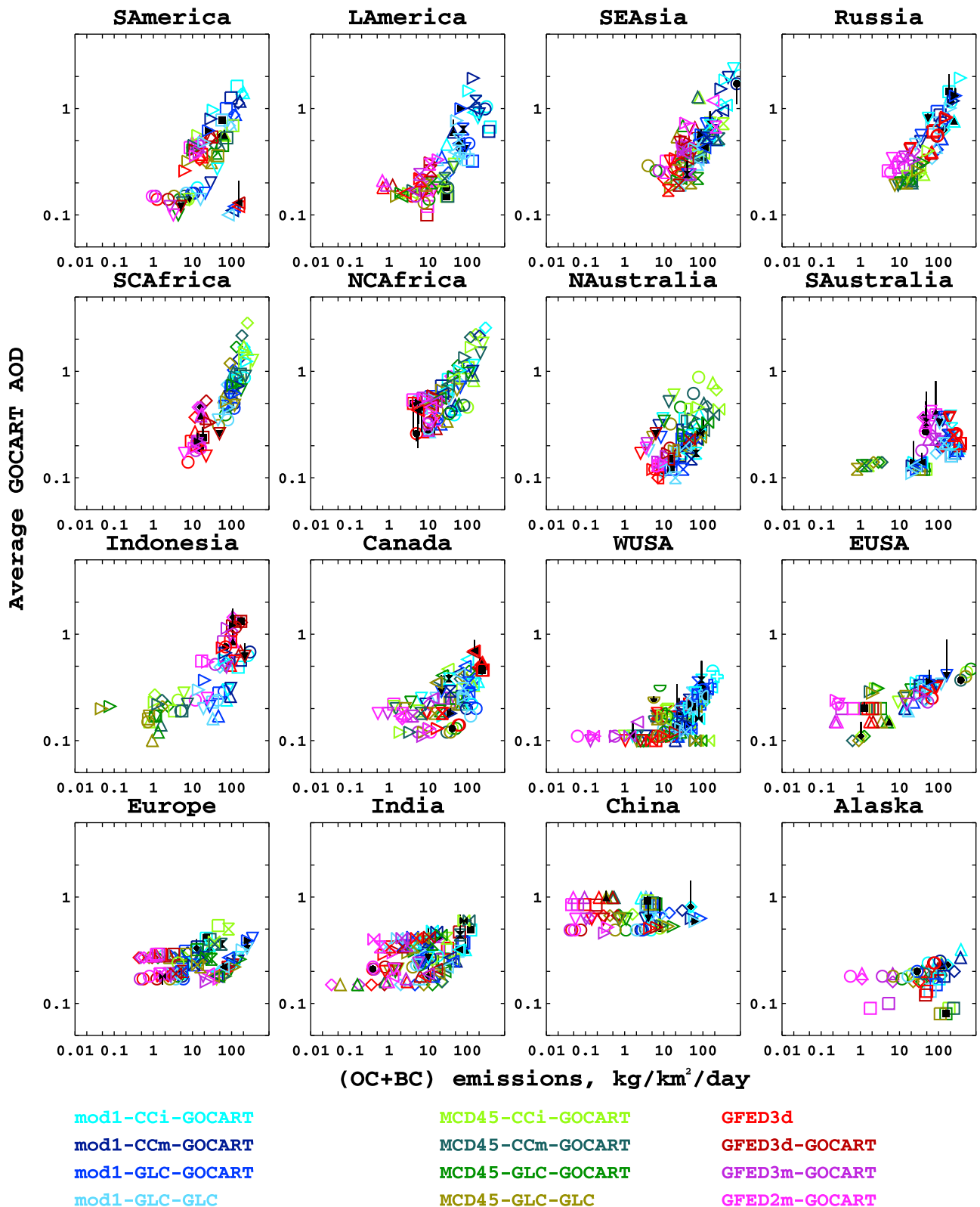


Figure 6. GOCART AOD versus average BC + OC emission rate. Different symbols distinguish individual fire cases (see Table 4). Colors represent different emission options in GOCART. The output of GOCART run for which the simulated AOD is closest to MODIS is marked in black. The black line from each such data point shows the magnitude of AOD underestimation or overestimation compared to the average MODIS AOD.

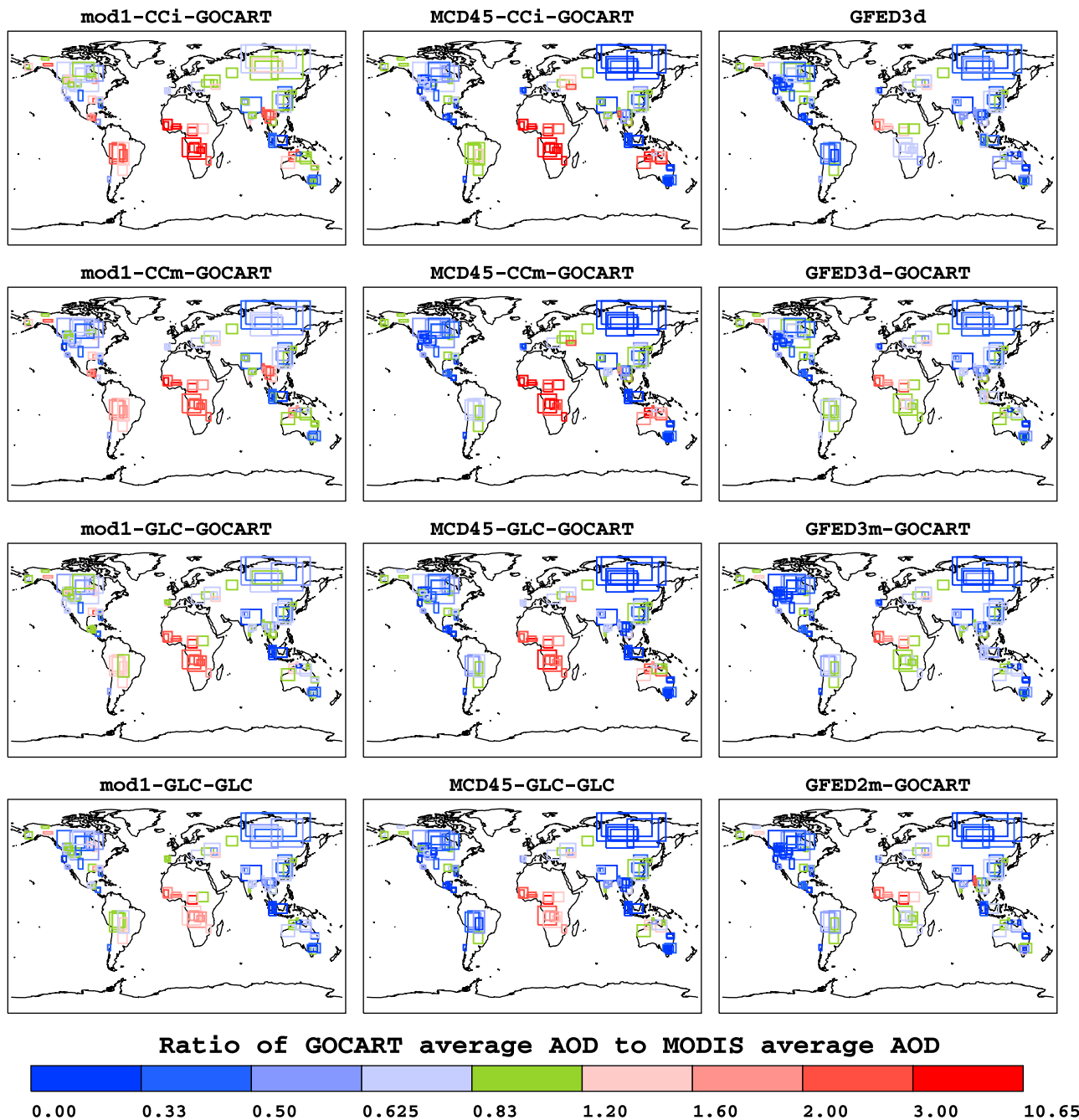


Figure 7. Ratios of GOCART average AOD to MODIS average AOD for each of the 124 studied cases, with different emission options used as input to GOCART.

[59] 1. The choice of MCD45-based emission options can lead to extreme AOD overestimation in the tropical regions of Africa and North Australia, and very low AOD values in the forest regions of Russia, Canada, Indonesia, and South Australia. These regional AOD trends compensate to produce average bias values of 0.5–0.85. However, the correlation coefficients are very low, emphasizing that the comparisons of AOD from MCD45-based GOCART runs and MODIS are non-uniform globally.

[60] 2. The correlation between mod1-based GOCART AOD and MODIS AOD is better than that for AOD with the MCD45-based emission options, and the mean bias is close

to unity, although from the clustering of data points in Figure 8, the compensation of high-AOD regions with low-AOD regions is apparent, but to a lesser extent than in MCD45-based model runs. As mentioned above, assuming 1 km² per fire count produces a higher-end estimate of burned area, and the “mod1”-based emission options tend to overestimate emissions, often by large factors in some regions (Latin and South America, Africa), but these high emission estimates bring simulated AOD close to MODIS-observed in the boreal regions.

[61] 3. Model runs using daily GFED3 emissions meet the criteria of higher R combined with lower RMSE and B close

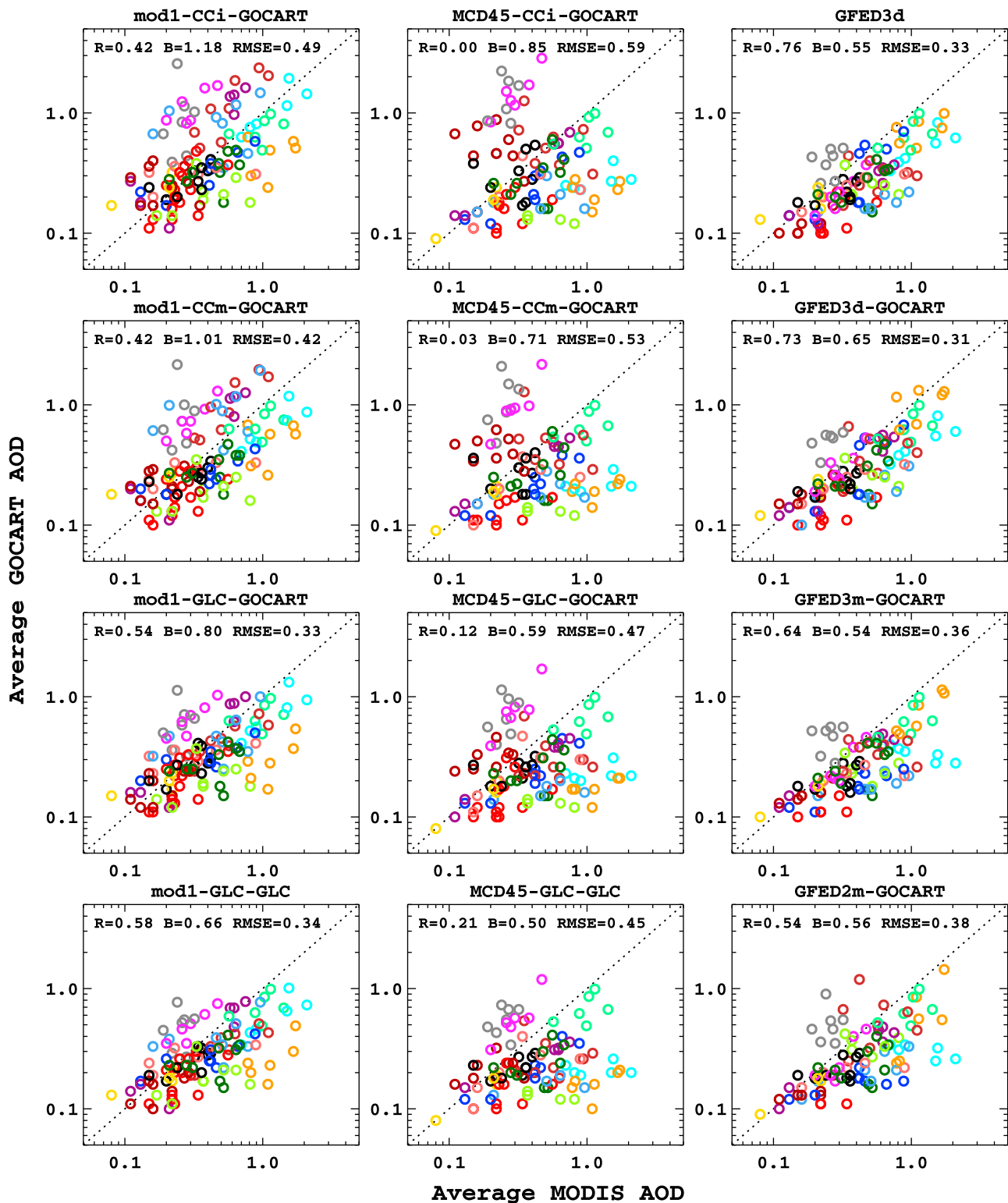


Figure 8. Average GOCART AOD versus average MODIS AOD for each of the 124 studied cases, with different emission options used as input to GOCART. The data points are colored according to the geographical location of the fire cases (Figure 1). Given for each panel are statistics of data set comparison: R is correlation coefficient, B is mean bias, and RMSE is root mean square error.

Table 5. Statistics of Average GOCART AOD Comparison With Average MODIS AOD for All Studied Fire Cases for Each BB Emission Option^a

BB Emission Option	R	B	E
Mod1-CCi-GOCART	0.42	1.18	0.49
Mod1-CCm-GOCART	0.42	1.01	0.42
Mod1-GLC-GOCART	0.54	0.80	0.33
Mod1-GLC-GLC	0.58	0.66	0.34
MCD45-CCi-GOCART	0.00	0.85	0.59
MCD45-CCm-GOCART	0.03	0.71	0.53
MCD45-GLC-GOCART	0.12	0.59	0.47
MCD45-GLC-GLC	0.21	0.50	0.45
GFED3d	0.76	0.55	0.33
GFED3d-GOCART	0.73	0.65	0.31
GFED3m-GOCART	0.64	0.54	0.36
GFED2m-GOCART	0.54	0.56	0.38

^aR is correlation coefficient, B is relative bias, and E is root mean square error.

to unity the best. The original GFED3 emission factors lead to a slightly larger correlation coefficient, but the use of GOCART emission factors is responsible for a smaller RMSE and not as low a bias. The use of GFED emission inventories generally leads to the best AOD comparison in Africa, where other inventories overestimate MODIS AOD, but in most other regions GFED-based model runs have AOD lower than MODIS, more so with monthly (GFEDv2, and GFED3) than daily inventories, as expected. Also as expected, monthly GFED inventories appear to perform well for the long-burning events in the sparsely vegetated regions of Africa, North Australia, South-East Asia, and tend to underestimate emissions more for intense individual fires in Russia, Canada, Indonesia and the USA.

[62] 4. Using the GFED3-daily emission inventory does not lead to a consistent improvement in all regions over monthly GFED3 estimates, but, as expected, it improves performance for shorter-lived fires. However, the larger

values of GOCART standard emission factors bring the emission estimates up, and closer to observations.

[63] To provide a more complete regional analysis, Figure 9 gives the geographic distribution of MODIS AOD associated with each fire. Examination of this figure together with Figures 7 and 8 suggests that in regions having average MODIS AOD 0.5 or larger, the simulated AOD tends to be lower than observed with most emission options used (except mod1-based options). These regions of higher AOD include Russia, South-East Asia, China, India, South Australia, as well as part of Latin America (Honduras), South America and Indonesia. In the regions with average MODIS AOD values of 0.5 or lower, the GOCART versus MODIS AOD comparison is less consistent.

[64] The persistent low bias of GOCART AOD in Indonesia, South Australia and Russia is immediately related to omissions in biomass burning emission estimates, because BB is the dominant source of aerosols in these regions. Model underestimation of total AOD in heavily pollution-dominated regions of India and China has been shown previously [Chin *et al.*, 2009], a problem that is mostly associated with the anthropogenic and dust emissions and transport.

[65] Qualitative comparison of the GOCART and MODIS AOD maps for the fire cases studied (only maps for case 11 are shown here in Figure 4) reveals that the model performs better spatially and more consistently in magnitude in the cases having large, distinct biomass burning plumes, such as the case in Russia shown in Figure 4. Thus, intense fires in the forested areas of Russia, Indonesia and Canada are best modeled by GOCART spatially, and the relative performance of the model is consistent from case to case when different emission inventories are used. These are the regions where the majority of emissions are only from BB sources and the plumes are significantly thick and distinct from the background. These are also regions of dark, densely vegetated surface, the best conditions for MODIS over-land AOD retrieval [Levy *et al.*, 2010].

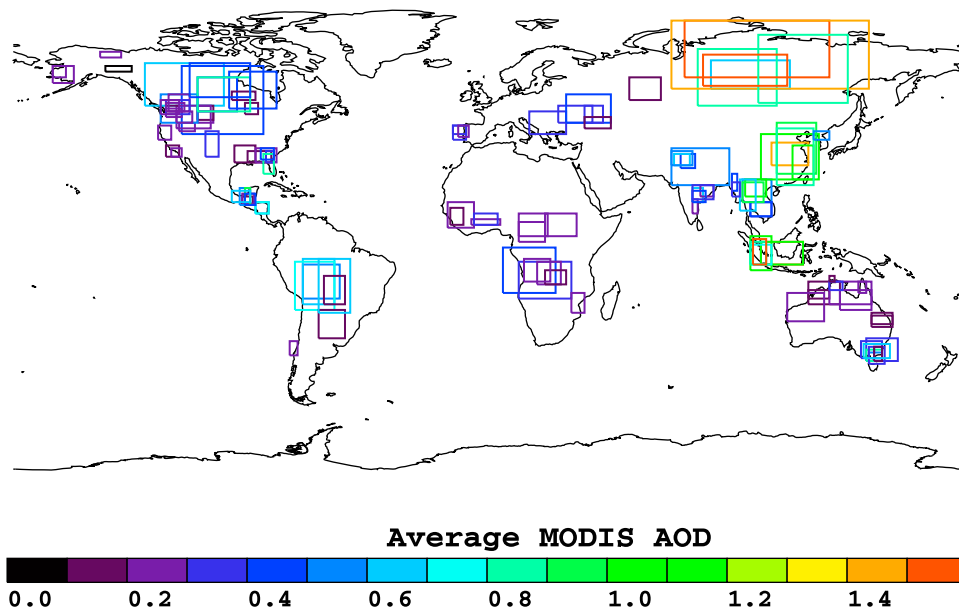


Figure 9. Average MODIS AOD of each of the 124 studied fire cases.

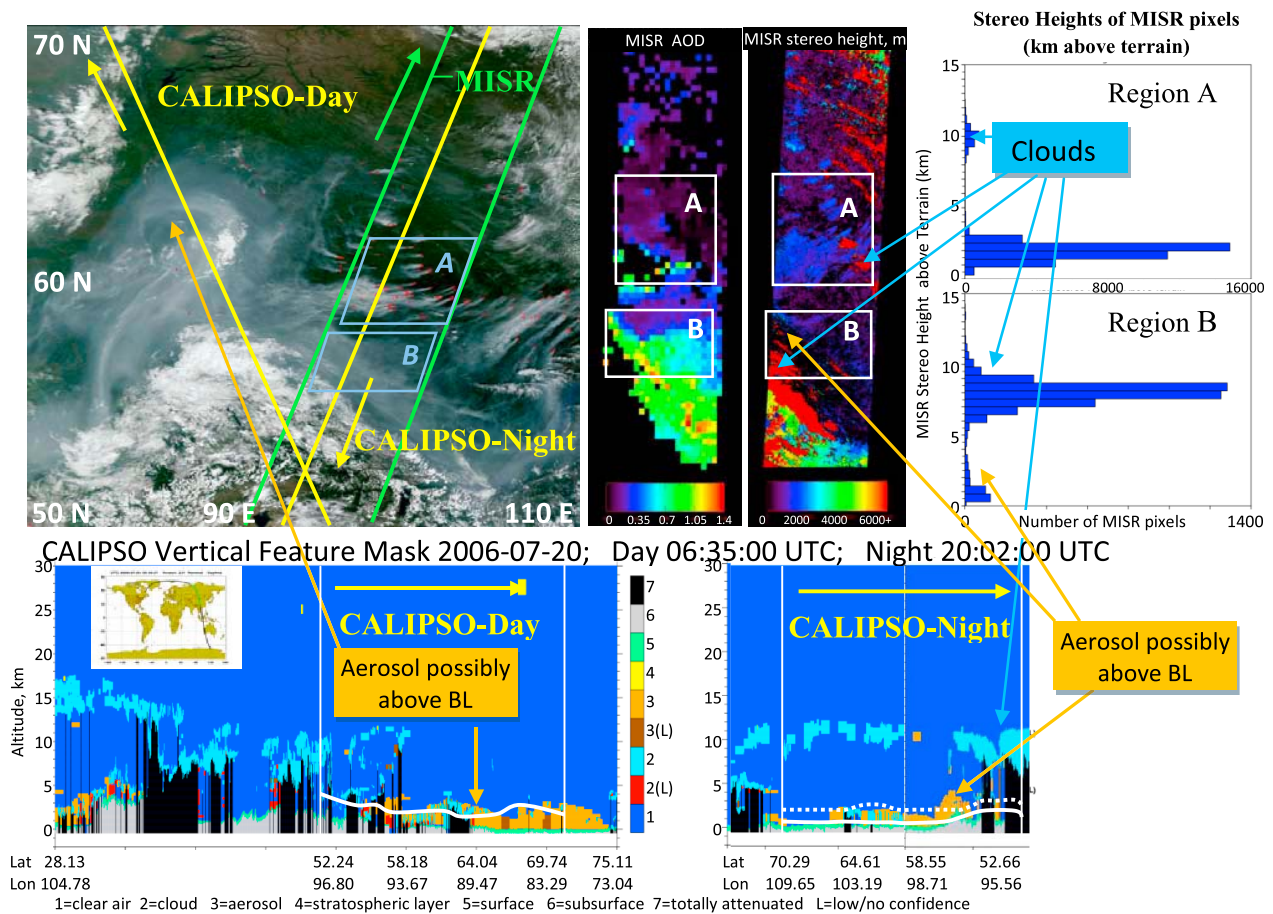


Figure 10. Case 11: Russia, 20 July 2006. (top) Terra-MODIS visible image of the scene with fire locations marked in red; schematic tracks of CALIPSO and MISR tracks during the same day in orange and light green, respectively. Satellites are moving in the direction marked with the arrows parallel to the orbits. Map of MISR Stereo heights, and the histograms of the pixel heights in two regions A (source region) and B (transported aerosol downwind) are shown. (bottom) CALIPSO Vertical feature mask overlaid by the GEOS-4 PBL height for the coordinates of the case box at the time of CALIPSO overpass. CALIPSO-Night observation also shows in dashed line the height of the mixing layer, approximated as the PBL height at 6:30 UTC (13:30 local time).

4.3. Effect of Aerosol Dispersion on AOD

[66] Spatial distribution of AOD depends not only on the source strength, but also on the rate at which the plume is dissipated. Therefore, to quantitatively evaluate the AOD-emissions relationship we have to account for smoke dissipation. Smoke plume dispersion is governed by wind shear and turbulence in the surrounding environment. Thus, strong vertical and horizontal atmospheric motions within the environment promote clear air entrainment, mixing, and plume dispersion. Plumes in stable air tend to stay more confined. Since smoke plume optical depth is proportional to smoke density, it is reasonable to assume that compact and well-contained plumes will be optically thicker than more dispersed plumes containing the same amount of aerosol particles. Therefore, in the BB-dominated regime, we expect similar changes in emission amount to have different effects on the resultant AOD when plume dispersion is different. We investigate the relationship between plume environment,

aerosol dispersion and their effects on simulated AOD values next.

4.3.1. Vertical Dispersion and Smoke Plume Height

[67] The spreading of smoke plumes in the vertical dimension reduces the aerosol concentration, which can reduce visibility through the plume, but has little effect on the plume AOD when seen from the top of the atmosphere. Additionally, if the smoke is injected directly into the free troposphere, the horizontal winds might transport it away fast enough to prevent accumulation of smoke, complicating the application of total AOD as a proxy for the cumulative strength of BB sources. Therefore, we checked whether the smoke was confined to the relatively well-mixed planetary boundary layer (PBL, as defined by GEOS4-DAS).

[68] The vertical structure of the smoke events studied was investigated by visually examining the MISR stereo height of the plumes or CALIPSO profiles whenever these observations were available. Figure 10 provides an example of how MISR and CALIPSO observations are used to find the

plume height. Both instruments passed over the plume in case 11 on the same day as MODIS. It is worth remembering that CALIPSO-Day measurement was made approximately 2.5 h after MISR, and CALIPSO-Night observation, spatially collocated with MISR, occurred about 16 h after the MISR and MODIS/Terra snapshots. The CALIPSO vertical feature mask is overlaid with the GEOS-4 PBL height, which is between about 2 and 3 km above terrain. Both CALIPSO aerosol profiles and histograms of MISR pixel heights indicate aerosol residing within the boundary layer, especially at the source, while detecting some higher clouds around 10 km. MISR heights away from the BB emission sources and CALIPSO-Day measurements have signatures of aerosol possibly transported above the PBL. PBL height being considerably lower at night, the height of the mixed layer, approximated by the PBL height at 6:30 A.M. UTC (13:30 local time), is also shown as a dashed line on the CALIPSO-Night plot in Figure 10.

[69] Although smoke injection above the PBL does occur in some cases, most smoke is emitted into the boundary layer [Kahn *et al.*, 2008; Val Martin *et al.*, 2010]. Out of 124 fire events studied here, we found smoke in the free troposphere only in a few large burning events in Russia, Canada, Indonesia and South Australia (cases 47, 48, 50, 2, 3, 14, 15, 16, 18, 20). Analysis similar to that shown in Figure 10 suggests the smoke was lifted there after initial injection into the boundary layer, and these cases conform to the general patterns described in the analysis sections below.

4.3.2. Horizontal Dispersion and Wind Speed

[70] To calculate average PBL wind speed for each case we average absolute mid-PBL wind speeds in all model grid boxes where the BB sources are defined. The same data points as in Figure 6 are plotted in Figure 11, now colored by the average PBL wind speed in the case box. A number of factors affect the apparent relationship between the AOD, which reflects the local concentration of aerosol particles, and the plume emission strength. We expect the AOD to be directly related to the emission strength, and inversely related to the local wind speed, which dissipates the aerosol. So other factors being equal, the slope of the AOD versus emission strength line would be steeper in cases having lower wind speeds, and shallower when the wind speed is higher. However, the atmospheric stability structure also affects the result, as the aerosol will tend to dissipate more readily in a less stable atmosphere, and if background aerosol dominates the emission source, the ambient AOD might not be significantly affected by changes in the strength of a local source, as discussed in Section 4.2 above.

4.4. Possibility of Using MODIS AOD as a Quantitative Constraint on Biomass Burning Aerosol Emissions

[71] To use satellite observation of AOD as a constraint to model emissions, a quantitative relationship must exist between the actual BB emission rate and MODIS-observed AOD, assuming that the GOCART model can reproduce this relationship. We have already established that wind speed is an important factor that governs the AOD-emissions relationship in BB-dominated regions. Therefore, we find a fit to the data points in the AOD versus emissions (BC + OC) plots for every region as is described below, and this relationship is the one needed to find the emission rate required to produce observed AOD in the given environmental

conditions. The GOCART average AOD closest to the MODIS average AOD for each case has been marked with a black symbol as in Figure 6, with a line from each such data point showing the magnitude of AOD under- or overestimation compared to the average MODIS AOD.

[72] An empirical emission density cutoff between background-dominated and BB-dominated regimes was chosen in each region where a BB-dominated regime is observed, and these cutoff values are listed in Table 6. The emission rate cutoff value is found to be around 10 kg/km²/day, where stronger emissions are likely to measurably affect the total column AOD, but varying depending on the background AOD. The data suggest that a larger cutoff value is required for India, probably due to a more polluted background, and a lower value in North Australia, for which there are no data clusters parallel to the x axis to form a background-dominated regime. No emission density cutoff could be selected for Alaska and China due to very faint plumes in the former (for the cases studied here) and a total domination of background aerosol in the latter.

[73] In each region, several lines, each corresponding to one of the three wind speed categories (0–3, 3–6, and >6 m/s) were fitted to the data points in the BB-dominated regime in Figure 11, corresponding to the linear fit of the form

$$Y = a + bX, \quad (3)$$

where X is the OC + BC daily integrated fire emission in kg per km², and Y is the average GOCART AOD within the plume. The resulting wind-regime-dependent regional fit coefficients a (intercept) and b (slope of the line), listed in Table 6, represent the level of background AOD and the rate of AOD change per unit change in BC + OC emission rate, respectively. Also listed in Table 6 are the fitted values of model AOD at the emissions density cutoff for this region. This value represents the background AOD, or the minimum plume AOD at which a smoke plume can be distinguished from its environment. The background AOD value averaged over all regions and wind speed regimes is about 0.26. The relationship between the manually chosen regional emission rate cutoff values, background AOD and the wind speed of the environment needs to be further explored, because the wind speed affects both the smoke plume and its environment. The slope of the fitted line, represented by the coefficient b , is steeper for the regions where a small increase in emissions leads to a noticeable increase in AOD. We also expect this slope to be steeper for lower wind speed regimes, since when dissipation is low, all the emitted particles contribute immediately to the plume AOD. The steepest slopes of the fitted lines are observed in South and Latin America and Africa, suggesting that even small errors in estimated emission rates will have noticeable effects on simulated AOD.

[74] The quantitative relationship between AOD and aerosol emission rate as a function of wind speed allows the use of MODIS AOD to constrain the BC + OC emission rate in the model, assuming the plume is emitted into the PBL and the average PBL wind speed is known. Such estimates should be more certain under lower wind speed conditions (due to small changes in emissions leading to significant changes in AOD), and less certain under higher wind speed conditions, where a larger range of emission rates is allowed within available constraints.

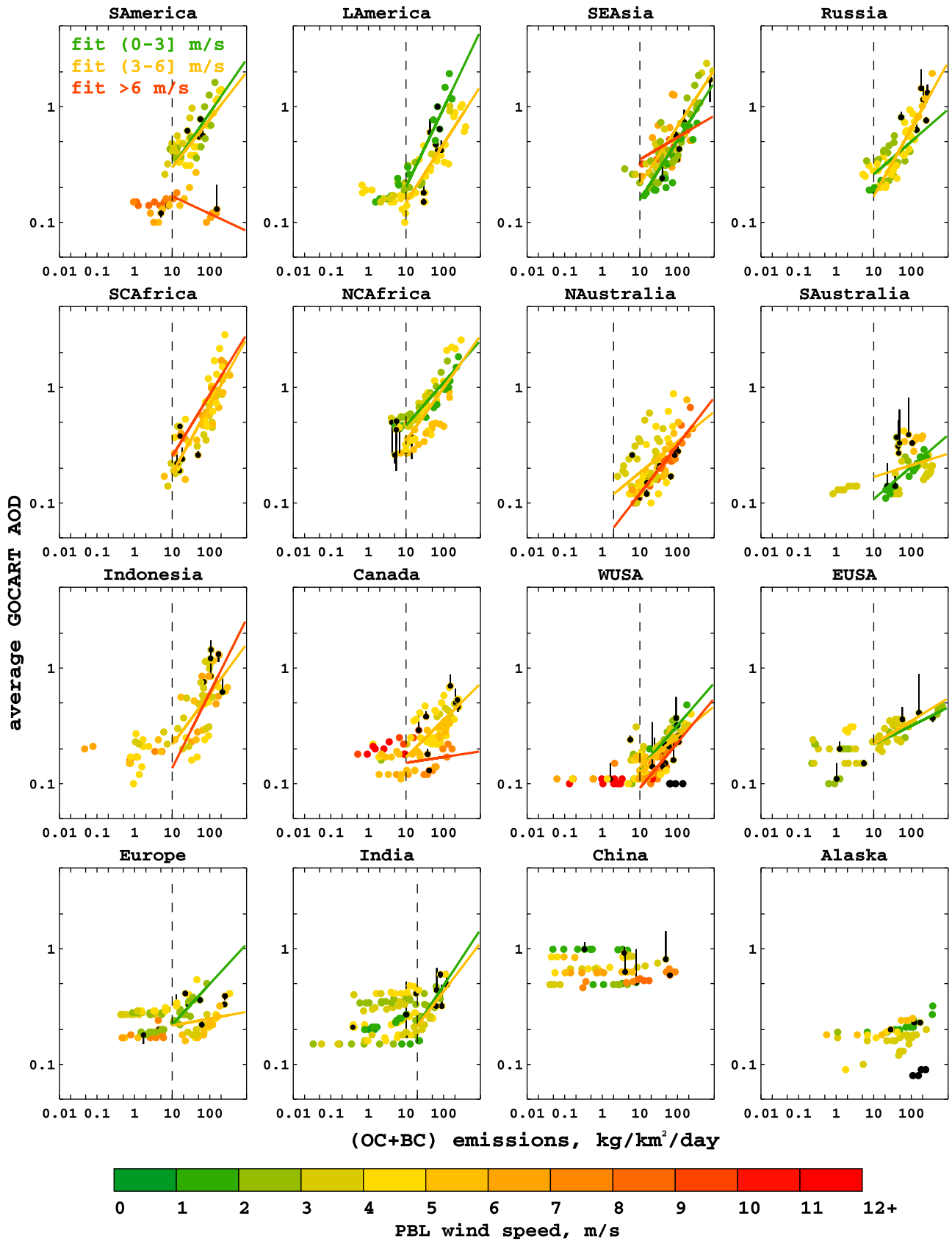


Figure 11. Same as Figure 6 but here the colors represent average PBL wind speed for each case at the BB source; the GOCART output closest to MODIS is marked in black.

Table 6. Regional Fit Coefficients for Equation (3) by Horizontal Wind Speed Range

Region	Emission Rate Cutoff (kg/m ² /day)	Fit Coefficients for Average Wind Speed Ranges					
		0–3 m/s		3–6 m/s		6+ m/s	
		a (AOD at Cutoff)	b ($\times 10^{-3}$)	a (AOD at Cutoff)	b ($\times 10^{-3}$)	a (AOD at Cutoff)	b ($\times 10^{-3}$)
SAmerica	10	0.20 (0.28)	8.3	0.30 (0.36)	5.2	0.16 (0.16)	–0.4
LAmerica	10	0.17 (0.26)	8.2	0.24 (0.26)	2.0		
SEAsia	10	0.20 (0.23)	2.8	0.35 (0.37)	2.3	0.48 (0.48)	0.7
Russia	10	0.29 (0.32)	2.3	0.18 (0.22)	4.4		
SCAfrica	10			0.17 (0.22)	5.3	0.22 (0.28)	6.0
NCAfrica	10	0.55 (0.60)	5.0	0.31 (0.39)	7.7		
NAustralia	2 ^a			0.16 (0.17)	3.0	0.12 (0.13)	1.8
SAustralia	10	0.15 (0.15)	0.5	0.24 (0.24)	0.0		
Indonesia	10			0.39 (0.41)	2.3	0.29 (0.32)	3.6
Canada	10			0.22 (0.23)	1.3	0.16 (0.16)	0.2
WUSA	10	0.14 (0.16)	1.9	0.15 (0.16)	1.0	0.09 (0.10)	1.7
EUSA	10	0.26 (0.26)	0.3	0.24 (0.25)	1.0		
Europe	10	0.21 (0.24)	3.6	0.22 (0.22)	0.4		
India	20	0.20 (0.25)	2.6	0.15 (0.22)	3.4		
China							
Alaska							

^aThe cutoff value was selected at the emission rate rounded to the full number near minimum AOD, because no data points clustered parallel to the x axis to form background-dominated regime.

4.5. Limitations of the Method and Topics for Further Study

[75] Our method of using MODIS AOD to constrain BB emissions in the global model has some limitations.

[76] 1. The method is based on the assumption that the discrepancies between MODIS and GOCART AOD are predominantly caused by the under- or over-estimation of emissions, such that the errors in aerosol removal or mass extinction efficiency (converting aerosol mass to AOD) are much smaller than that in emissions. This assumption could be wrong in some cases.

[77] 2. It has been shown that total column AOD provides a poor constraint on BB emissions in background-dominated regions.

[78] 3. The effect of wind speed on the AOD-emissions relationship has to be explored further in the light of interaction of smoke plume with more or less polluted environment.

[79] 4. Even though physically sound, the relationship between AOD and BB aerosol emission rate has been quantitatively described for one version of the GOCART model only, and its application to models having different spatial resolution and physical aerosol processes needs to be investigated.

[80] 5. The use of the MODIS AOD product brings its own limitations, such as missing AOD retrievals in the cores of very optically thick plumes, over bright surfaces, or in regions with complex cloud cover, and AOD over- or underestimation in some situations [Levy *et al.*, 2010]. Model bias in some regions, such as low bias in the Western U.S., Asia and India or high bias in Northern Africa can be related to known anomalies in the MODIS AOD product. Previous MODIS AOD validation studies showed that MODIS tends to overestimate AOD in the Western U.S., Central Asia and India, and to underestimate AOD in Northern Africa, South America and Northern Australia [Levy *et al.*, 2010; Hyer *et al.*, 2011]. Therefore, the magnitude of differences between the GOCART AOD and MODIS AOD in these regions may not be as large as what is

reported here, and merits a more in-depth investigation, possibly using other AOD data sets such as MISR for model validation.

[81] 6. The results in this study are based on one year of fire observations. Inter-annual variability of fire locations and intensity merits further investigation, to test the applicability of the method quantitatively in regions where fire seasons, and thus, fire and smoke properties and amount, can vary significantly.

[82] 7. Since the global model is too coarse to simulate individual smoke plumes of sub-grid size, the method is rendered insensitive to small AOD variations when averaging MODIS AOD, and is similarly insensitive to small aerosol concentration changes, when the model requires an aerosol emission source the size of an entire grid box.

5. Conclusions

[83] We used ready-to-use global biomass burning aerosol emission inventories GFEDv2, GFED3, and QFED, as well as several combinations of burned area, effective fuel load and aerosol emission factor estimates for this study, which resulted in a total of thirteen global BB emission options. We compared the amounts of BB aerosol emitted during the year 2006, as estimated by all thirteen emission options, and found that annual global total BC or OC emission estimates can differ by up to a factor of eight, with GFED3 providing the lowest estimate, and emission options based on MODIS fire counts, Langley Carbon Consumption estimates and GOCART emission factors producing the largest. Although emission factor and effective fuel load choices can each lead to about a factor of two-to-three difference in a given region, burned area estimates can vary dramatically between the inventories, producing the largest differences between emission options. The performance of these emission options in the GOCART model was evaluated by comparing model simulated AOD to the MODIS-measured AOD. AOD from QFED-based model runs could not be fairly used in

such comparison, due to the use of MODIS AOD as one of the parameters in calibrating QFED emissions.

[84] Twelve GOCART runs, each with a different emission option, comprise an ensemble of runs, providing a range of input emissions and output AOD estimates that were evaluated for 124 fire events chosen globally. In general, the model performs best spatially and most consistently in magnitude when simulating large biomass burning events of Russia and Canada, and less consistently in the regions where other sources of aerosol, such as anthropogenic pollution or dust, make significant contributions to the background - Asia, Africa, Central-Eastern Europe. In regions of complex terrain and patchy vegetation, such as the USA, the inventories do not agree well, and the comparison between GOCART and MODIS is not consistent.

[85] The use of GFED inventories leads to the best AOD agreement in Africa, where other inventories overestimate MODIS AOD, but in most other regions GFED-based runs have lower-than-MODIS AOD. The use of daily GFED emissions generally improves AOD comparison compared to the use of monthly emission estimates in the cases of short-lived individual fires. Emission estimates based on MCD45 burned area lead to significant AOD underestimation in higher latitudes, and overestimation in Africa. 'mod1'-based model runs result in the best AOD comparisons in the boreal regions, while mostly overestimating AOD in the tropical regions.

[86] The relationship between BB aerosol, expressed as a sum of BC and OC emissions, and the resultant AOD, forms two distinct regimes. First is the "BB-dominated" regime where BB is the main aerosol source, and changes in BB emission rate clearly affect the total AOD in the region. Second is the "background-dominated" regime, in which the contribution of BB smoke to the total AOD is small enough that changes in smoke emission rate do not produce significant total-AOD changes. The rate of BC + OC emission from BB (in units of $\text{kg}/\text{km}^2/\text{day}$) needs to be larger than a certain threshold for emission-AOD relationship to be in BB-dominated regime. This threshold is around $10 \text{ kg}/\text{km}^2/\text{day}$ in most regions studied, when the source is of the size of the GOCART model grid box, but varies depending on the background AOD level.

[87] The rate of change of AOD in response to changes in amount of BB emissions is affected by the dispersion potential of the plume environment, which is usually dominated by the wind speed and atmospheric stability. In clean environments, higher wind speeds lead to shallower slopes of the AOD versus emissions relationship, meaning larger changes in AOD are needed to noticeably affect the total column AOD. Thus, given a quantitative relationship between AOD and BB emissions in each geographic region, satellite-measured AOD can be used to constrain the BB source strength, given the average wind speed in the region. However, MODIS total column AOD cannot be used to constrain BB emissions in the background-dominated regime, and the regional quality of the MODIS AOD product also has to be considered when using it as a quantitative constraint.

[88] **Acknowledgments.** We thank Catherine Lioussé for providing GLC2000 effective fuel load files and emission factors, Anton Darnenov and Arlindo da Silva for providing access to QFED emission data set, Matthew Davis and James Limbacher for software support when processing satellite data products, and Thomas Diehl and Qian Tan for help with

configuring the GOCART model. We thank the reviewers for providing very useful and insightful comments, that helped improve this manuscript. This work was funded primarily by NASA grants NNX08AU81H and NNX10AG61G to Purdue University. The work of R. Kahn is supported in part by NASA's Atmospheric Composition Program, NASA's Climate and Radiation Research and Analysis Program under H. Maring, and the EOS MISR project.

References

- Akagi, S. K., R. J. Yokelson, C. Wiedinmyer, M. J. Alvarado, J. S. Reid, T. Karl, J. D. Crouse, and P. O. Wennberg (2011), Emission factors for open and domestic biomass burning for use in atmospheric models, *Atmos. Chem. Phys.*, *11*, 4039–4072, doi:10.5194/acp-11-4039-2011.
- Al-Saadi, J., et al. (2008), Intercomparison of near-real-time biomass burning emissions estimates constrained by satellite fire data, *J. Appl. Remote Sens.*, *2*, 021504.
- Alexeyev, V. A., and R. A. Birdsey (1998), Carbon storage in forests and peatlands of Russia, *Gen. Tech. Rep. NE-244*, 137 pp., For. Serv., U.S. Dep. of Agric., Radnor, Penn.
- Andreae, M. O., and P. Merlet (2001), Emission of trace gases and aerosols from biomass burning, *Global Biogeochem. Cycles*, *15*(4), 955–966, doi:10.1029/2000GB001382.
- Andreae, M. O., et al. (1988), Biomass-burning emissions and associated haze layers over Amazonia, *J. Geophys. Res.*, *93*(D2), 1509–1527, doi:10.1029/JD093iD02p01509.
- Bartholomé, E., and A. S. Belward (2005), GLC2000: A new approach to global land cover mapping from Earth observation data, *Int. J. Remote Sens.*, *26*(9), 1959–1977, doi:10.1080/01431160412331291297.
- Bäumler, D., B. Vogelb, S. Versickb, R. Rinkeb, O. Möhlerb, and M. Schnaiter (2008), Relationship of visibility, aerosol optical thickness and aerosol size distribution in an ageing air mass over South-West Germany, *Atmos. Environ.*, *42*(5), 989–998, doi:10.1016/j.atmosenv.2007.10.017.
- Bloom, S., et al. (2005), Documentation and validation of the Goddard Earth Observing System (GEOS) data assimilation system, version 4, *Rep. NASA/TM-2005-104606*, NASA Goddard Space Flight Cent., Greenbelt, Md.
- Boucher, O., and T. L. Anderson (1995), General circulation model assessment of the sensitivity of direct climate forcing by anthropogenic sulfate aerosols to aerosol size and chemistry, *J. Geophys. Res.*, *100*(D12), 26,117–26,134, doi:10.1029/95JD02531.
- Chen, Y., Q. Li, J. T. Randerson, E. A. Lyons, R. A. Kahn, D. L. Nelson, and D. J. Diner (2009), The sensitivity of CO and aerosol transport to the temporal and vertical distribution of North American boreal fire emissions, *Atmos. Chem. Phys.*, *9*, 6559–6580, doi:10.5194/acp-9-6559-2009.
- Chin, M., R. B. Rood, S.-J. Lin, J.-F. Muller, and A. M. Thompson (2000), Atmospheric sulfur cycle simulated in the global model GOCART: Model description and global properties, *J. Geophys. Res.*, *105*(D20), 24,671–24,687, doi:10.1029/2000JD900384.
- Chin, M., P. Ginoux, S. Kinne, O. Torres, B. N. Holben, B. N. Duncan, R. V. Martin, J. A. Logan, A. Higurashi, and T. Nakajima (2002), Tropospheric aerosol optical thickness from the GOCART model and comparisons with satellite and Sun photometer measurements, *J. Atmos. Sci.*, *59*, 461–483, doi:10.1175/1520-0469(2002)059<0461:TAOTFT>2.0.CO;2.
- Chin, M., A. Chu, R. Levy, L. Remer, Y. Kaufman, B. Holben, T. Eck, P. Ginoux, and Q. Gao (2004), Aerosol distribution in the Northern Hemisphere during ACE-Asia: Results from global model, satellite observations, and Sun photometer measurements, *J. Geophys. Res.*, *109*, D23S90, doi:10.1029/2004JD004829.
- Chin, M., T. Diehl, P. Ginoux, and W. Malm (2007), Intercontinental transport of pollution and dust aerosols: Implications for regional air quality, *Atmos. Chem. Phys.*, *7*, 5501–5517, doi:10.5194/acp-7-5501-2007.
- Chin, M., T. Diehl, O. Dubovik, T. F. Eck, B. N. Holben, A. Sinyuk, and D. G. Streets (2009), Light absorption by pollution, dust, and biomass burning aerosols: A global model study and evaluation with AERONET measurements, *Ann. Geophys.*, *27*, 3439–3464, doi:10.5194/angeo-27-3439-2009.
- Choi, Y., et al. (2008), Characteristics of the atmospheric CO₂ signal as observed over the conterminous United States during INTEX-NA, *J. Geophys. Res.*, *113*, D07301, doi:10.1029/2007JD008899.
- Climate Change Science Program Working Group (2009), Atmospheric aerosol properties and climate impacts: A report by the U.S. Climate Change Science Program and the subcommittee on global change research, report, NASA, Washington, D. C.
- Colarco, P. R., M. R. Schoeberl, B. G. Doddridge, L. T. Marufu, O. Torres, and E. J. Welton (2004), Transport of smoke from Canadian forest fires to the surface near Washington, D.C.: Injection height, entrainment, and optical properties, *J. Geophys. Res.*, *109*, D06203, doi:10.1029/2003JD004248.

- Damoah, R., N. Spichtinger, C. Forster, P. James, I. Mattis, U. Wandinger, S. Beirle, T. Wagner, and A. Stohl (2004), Around the world in 17 days—hemispheric-scale transport of forest fire smoke from Russia in May 2003, *Atmos. Chem. Phys.*, *4*, 1311–1321, doi:10.5194/acp-4-1311-2004.
- Dentener, F., D. Stevenson, J. Cofala, R. Mechler, M. Amann, P. Bergamaschi, F. Raes, and R. Derwent (2005), The impact of air pollutant and methane emission controls on tropospheric ozone and radiative forcing: CTM calculations for the period 1990–2030, *Atmos. Chem. Phys.*, *5*, 1731–1755, doi:10.5194/acp-5-1731-2005.
- Dentener, F., et al. (2006), Emissions of primary aerosol and precursor gases in the years 2000 and 1750 prescribed data-sets for AeroCom, *Atmos. Chem. Phys.*, *6*, 4321–4344, doi:10.5194/acp-6-4321-2006.
- Dey, S., and L. Di Girolamo (2010), A climatology of aerosol optical and microphysical properties over the Indian subcontinent from 9 years (2000–2008) of Multiangle Imaging Spectroradiometer (MISR) data, *J. Geophys. Res.*, *115*, D15204, doi:10.1029/2009JD013395.
- Diner, D. J., et al. (1998), Multi-angle Imaging Spectroradiometer (MISR) instrument description and experiment overview, *IEEE Trans. Geosci. Remote Sens.*, *36*(4), 1072–1087, doi:10.1109/36.700992.
- Dubovik, O., T. Lapyonok, Y. J. Kaufman, M. Chin, P. Ginoux, R. A. Kahn, and A. Sinyuk (2008), Retrieving global aerosol sources from satellites using inverse modeling, *Atmos. Chem. Phys.*, *8*, 209–250, doi:10.5194/acp-8-209-2008.
- Duncan, B. N., R. V. Martin, A. C. Staudt, R. Yevich, and J. Logan (2003), Interannual and seasonal variability of biomass burning emissions constrained by satellite observations, *J. Geophys. Res.*, *108*(D2), 4100, doi:10.1029/2002JD002378.
- Eyring, V., H. W. Kohler, J. V. Aardenne, and A. Lauer (2005), Emissions from international shipping: 1. The last 50 years, *J. Geophys. Res.*, *110*, D17305, doi:10.1029/2004JD005619.
- Freitas, S. R., K. M. Longo, and M. O. Andreae (2006), Impact of including the plume rise of vegetation fires in numerical simulations of associated atmospheric pollutants, *Geophys. Res. Lett.*, *33*, L17808, doi:10.1029/2006GL026608.
- Fritz, S., and L. See (2008), Identifying and quantifying uncertainty and spatial disagreement in the comparison of global land cover for different applications, *Global Change Biol.*, *14*, 1057–1075, doi:10.1111/j.1365-2486.2007.01519.x.
- Giglio, L. (2010), MODIS collection 5 active fire product user's guide version 2.4, report, NASA Goddard Space Flight Cent., Greenbelt, Md.
- Giglio, L., I. Csizsar, and C. O. Justice (2006a), Global distribution and seasonality of active fires as observed with the Terra and Aqua Moderate Resolution Imaging Spectroradiometer (MODIS) sensors, *J. Geophys. Res.*, *111*, G02016, doi:10.1029/2005JG000142.
- Giglio, L., G. R. van der Werf, J. T. Randerson, G. J. Collatz, and P. Kasibhatla (2006b), Global estimation of burned area using MODIS active fire observations, *Atmos. Chem. Phys.*, *6*, 957–974, doi:10.5194/acp-6-957-2006.
- Giglio, L., T. Loboda, D. P. Roy, B. Quayle, and C. O. Justice (2009), An active-fire based burned area mapping algorithm for the MODIS sensor, *Remote Sens. Environ.*, *113*, 408–420, doi:10.1016/j.rse.2008.10.006.
- Giglio, L., J. T. Randerson, G. R. V. derWerf, P. S. Kasibhatla, G. J. Collatz, D. C. Morton, and R. S. DeFries (2010), Assessing variability and long-term trends in burned area by merging multiple satellite fire products, *Biogeosciences*, *7*, 1171–1186, doi:10.5194/bg-7-1171-2010.
- Ginoux, P., M. Chin, I. Tegen, J. M. Prospero, B. Holben, O. Dubovik, and S.-J. Lin (2001), Sources and distributions of dust aerosols simulated with the GOCART model, *J. Geophys. Res.*, *106*(D17), 20,255–20,273, doi:10.1029/2000JD000053.
- Gonsamo, A., and J. M. Chen (2011), Evaluation of the GLC2000 and NALC2005 land cover products for LAI retrieval over Canada, *Can. J. Rem. Sens.*, *37*(3), 302–313, doi:10.5589/m11-039.
- Haines, D. A. (1988), A lower atmosphere severity index for wildland fires, *Natl. Weather Digest*, *13*, 23–27.
- Hyer, E. J., and J. S. Reid (2009), Baseline uncertainties in biomass burning emission models resulting from spatial error in satellite active fire location data, *Geophys. Res. Lett.*, *36*, L05802, doi:10.1029/2008GL036767.
- Hyer, E. J., D. J. Allen, and E. S. Kasischke (2007), Examining injection properties of boreal forest fires using surface and satellite measurements of CO transport, *J. Geophys. Res.*, *112*, D18307, doi:10.1029/2006JD008232.
- Hyer, E. J., J. S. Reid, and J. Zhang (2011), An over-land aerosol optical depth data set for data assimilation by filtering, correction, and aggregation of MODIS Collection 5 optical depth retrievals, *Atmos. Meas. Tech.*, *4*, 379–408, doi:10.5194/amt-4-379-2011.
- Ichoku, C., and Y. Kaufman (2005), A method to derive smoke emission rates from MODIS fire radiative energy measurements, *IEEE Trans. Geosci. Remote Sens.*, *43*(11), 2636–2649, doi:10.1109/TGRS.2005.857328.
- Ito, A., and J. E. Penner (2004), Global estimates of biomass burning emissions based on satellite imagery for the year 2000, *J. Geophys. Res.*, *109*, D14S05, doi:10.1029/2003JD004423.
- Jaffé, D., I. Bertschi, L. Jaeglé, P. Novelli, J. S. Reid, H. Tanimoto, R. Vingarzan, and D. L. Westphal (2004), Long-range transport of Siberian biomass burning emissions and impact on surface ozone in western North America, *Geophys. Res. Lett.*, *31*, L16106, doi:10.1029/2004GL020093.
- Kahn, R. A., W.-H. Li, C. Moroney, D. J. Diner, J. V. Martonchik, and E. Fishbein (2007), Aerosol source plume physical characteristics from space-based multiangle imaging, *J. Geophys. Res.*, *112*, D11205, doi:10.1029/2006JD007647.
- Kahn, R. A., Y. Chen, D. L. Nelson, F.-Y. Leung, Q. Li, D. J. Diner, and J. A. Logan (2008), Wildfire smoke injection heights: Two perspectives from space, *Geophys. Res. Lett.*, *35*, L04809, doi:10.1029/2007GL032165.
- Kahn, R. A., B. J. Gaitley, M. J. Garay, D. J. Diner, T. F. Eck, A. Smirnov, and B. N. Holben (2010), Multiangle Imaging Spectroradiometer global aerosol product assessment by comparison with the Aerosol Robotic Network, *J. Geophys. Res.*, *115*, D23209, doi:10.1029/2010JD014601.
- Kaiser, J. W., et al. (2012), Biomass burning emissions estimated with a global fire assimilation system based on observed fire radiative power, *Biogeosciences*, *9*, 527–554, doi:10.5194/bg-9-527-2012.
- Kaufman, Y., L. Remer, R. Ottmar, D. Ward, L. Rong-R., R. Kleidman, R. Fraser, L. Flynn, D. McDougal, and G. Shelton (1996), Relationship between remotely sensed fire intensity and rate of emission of smoke: SCAR-C experiment, in *Global Biomass Burning*, edited by J. Levine, pp. 685–696, MIT Press, Cambridge, Mass.
- Levy, R. C., L. A. Remer, and O. Dubovik (2007), Global aerosol optical properties and application to Moderate Resolution Imaging Spectroradiometer aerosol retrieval over land, *J. Geophys. Res.*, *112*, D13210, doi:10.1029/2006JD007815.
- Levy, R. C., L. A. Remer, R. G. Kleidman, S. Mattoo, C. Ichoku, R. Kahn, and T. F. Eck (2010), Global evaluation of the Collection 5 MODIS dark-target aerosol products over land, *Atmos. Chem. Phys.*, *10*, 10,399–10,420, doi:10.5194/acp-10-10399-2010.
- Lioussé, C., et al. (2004), Deriving global quantitative estimates for spatial and temporal distributions of biomass burning emissions, in *Emissions of Atmospheric Trace Compounds*, *Adv. Global Change Res.*, vol. 18, edited by C. Granier, P. Artaxo, and C. Reeves, pp. 71–114, Kluwer Acad., Dordrecht, Netherlands.
- Lioussé, C., et al. (2010), Updated African biomass burning emission inventories in the framework of the AMMA-IDAF program, with an evaluation of combustion aerosols, *Atmos. Chem. Phys.*, *10*, 9631–9646, doi:10.5194/acp-10-9631-2010.
- Lohmann, U., and J. Feichter (2005), Global indirect aerosol effects: A review, *Atmos. Chem. Phys.*, *5*, 715–737, doi:10.5194/acp-5-715-2005.
- Mazurek, M., M. C. Masonjones, H. D. Masonjones, L. G. Salmon, G. R. Cass, K. A. Hallock, and M. Leach (1997), Visibility-reducing organic aerosols in the vicinity of Grand Canyon National Park: Properties observed by high resolution gas chromatography, *J. Geophys. Res.*, *102*(D3), 3779–3793, doi:10.1029/96JD02719.
- McMurray, P., M. Shepherd, and J. Vickery (Eds.) (2004), *Particulate Matter Science for Policy Makers: A NARSTO Assessment*, 510 pp., Cambridge Univ. Press, Cambridge, U. K.
- Michel, C., C. Lioussé, J.-M. Grégoire, K. Tansey, G. R. Carmichael, and J.-H. Woo (2005), Biomass burning emission inventory from burnt area data given by the SPOT-VEGETATION system in the frame of TRACE-P and ACE-Asia campaigns, *J. Geophys. Res.*, *110*, D09304, doi:10.1029/2004JD005461.
- Moroney, C., R. Davies, and J.-P. Muller (2002), Operational retrieval of cloud-top heights using MISR data, *IEEE Trans. Geosci. Remote Sens.*, *40*(7), 1532–1540, doi:10.1109/TGRS.2002.801150.
- Mortlock, A. M., and R. Van Alstyne (1998), Military, charter, unreported domestic traffic and general aviation 1976, 1984, 1992, and 2015 emissions scenarios, *Rep. NASA/CR-1998-207639*, NASA, Hampton, Va.
- Mu, M., et al. (2011), Daily and hourly variability in global fire emissions and consequences for atmospheric model predictions of carbon monoxide, *J. Geophys. Res.*, *116*, D24303, doi:10.1029/2011JD016245.
- Olson, J. S., R. M. Garrels, R. A. Berner, T. V. Armentano, M. I. Dyer, and D. H. Taalon (1985), The natural carbon cycle, in *Atmospheric Carbon Dioxide and the Global Carbon Cycle*, edited by J. R. Trabalka, pp. 175–213, U.S. Dep. of Energy, Washington, D. C.
- Pandithurai, G., R. T. Pinker, O. Dubovik, B. N. Holben, and T. O. Aro (2001), Remote sensing of aerosol optical characteristics in sub-Saharan West Africa, *J. Geophys. Res.*, *106*(D22), 28,347–28,356, doi:10.1029/2001JD00234.
- Patterson, E. M., C. K. McMahon, and D. Ward (1986), Absorption properties and graphitic carbon emission factors of forest fire aerosols, *Geophys. Res. Lett.*, *13*(2), 129–132, doi:10.1029/GL013i002p00129.
- Pierce, R. B., et al. (2007), Chemical data assimilation estimates of continental U.S. ozone and nitrogen budgets during the Intercontinental Chemical Transport Experiment—North America, *J. Geophys. Res.*, *112*, D12S21, doi:10.1029/2006JD007722.

- Quinn, P. K., et al. (2008), Short-lived pollutants in the Arctic: Their climate impact and possible mitigation strategies, *Atmos. Chem. Phys.*, *8*, 1723–1735, doi:10.5194/acp-8-1723-2008.
- Reid, J. S., et al. (2009), Global monitoring and forecasting of biomass-burning smoke: Description of and lessons from the Fire Locating and Modeling of Burning Emissions (FLAMBE) program, *IEEE J. Sel. Topics Appl. Earth Observ. Remote Sens.*, *2*(3), 144–162, doi:10.1109/JSTARS.2009.2027443.
- Remer, L. A., D. Tanré, Y. J. Kaufman, R. Levy, and S. Mattoo (2006), Algorithm for remote sensing of tropospheric aerosol from MODIS: Collection 5. Product ID: MOD04/MYD04, report, NASA Goddard Space Flight Cent., Greenbelt, Md.
- Rienecker, M. M., et al. (2008), The GEOS-5 Data Assimilation System—Documentation of versions 5.0.1, 5.1.0, and 5.2.0, report, NASA Goddard Space Flight Cent., Greenbelt, Md.
- Roy, D. P., L. Boschetti, C. O. Justice, and J. Ju (2008), The collection 5 MODIS burned area product—Global evaluation by comparison with the MODIS active fire product, *Remote Sens. Environ.*, *112*, 3690–3707, doi:10.1016/j.rse.2008.05.013.
- Sapkota, A., J. M. Symons, J. Kleissl, L. Wang, M. B. Parlange, J. Ondov, P. N. Breyse, G. B. Diette, P. A. Eggleston, and T. J. Buckley (2005), Impact of the 2002 Canadian forest fires on particulate matter air quality in Baltimore city, *Environ. Sci. Technol.*, *39*, 24–32, doi:10.1021/es035311z.
- Schroeder, W., I. Csiszar, L. Giglio, and C. C. Schmidt (2010), On the use of fire radiative power, area, and temperature estimates to characterize biomass burning via moderate to coarse spatial resolution remote sensing data in the Brazilian Amazon, *J. Geophys. Res.*, *115*, D21121, doi:10.1029/2009JD013769.
- Schultz, M. G., A. Heil, J. J. Hoelzemann, A. Spessa, K. Thonicke, J. Goldammer, A. C. Held, and J. M. Pereira (2008), Global emissions from wildland fires from 1960 to 2000, *Global Biogeochem. Cycles*, *22*, GB2002, doi:10.1029/2007GB003031.
- Seaton, A., D. Godden, W. MacNee, and K. Donaldson (1995), Particulate air pollution and acute health effects, *Lancet*, *345*(8943), 176–178, doi:10.1016/S0140-6736(95)90173-6.
- See, L. M., and S. Fritz (2006), A method to compare and improve land cover datasets: Application to the GLC-2000 and MODIS land cover products, *IEEE Trans. Geosci. Remote Sens.*, *44*(7), 1740–1746, doi:10.1109/TGRS.2006.874750.
- Seiler, W., and P. J. Crutzen (1980), Estimates of gross and net fluxes of carbon between the biosphere and the atmosphere from biomass burning, *Clim. Change*, *2*, 207–247, doi:10.1007/BF00137988.
- Seinfeld, J. H., and S. N. Pandis (1998), *Atmospheric Chemistry and Physics: From Air Pollution to Climate Change*, John Wiley, New York.
- Sessions, W. R., H. E. Fuelberg, R. A. Kahn, and D. M. Winker (2011), An investigation of methods for injecting emissions from boreal wildfires using WRF-Chem during ARCTAS, *Atmos. Chem. Phys.*, *11*, 5719–5744, doi:10.5194/acp-11-5719-2011.
- Shindell, D., J.-F. Lamarque, N. Unger, D. Koch, G. Faluveg, S. Bauer, and H. Teich (2008), Climate forcing and air quality change due to regional emissions reductions by economic sector, *Atmos. Chem. Phys.*, *8*, 7101–7113, doi:10.5194/acp-8-7101-2008.
- Soja, A. J., W. R. Cofer, H. H. Shugart, A. I. Sukhinin, P. W. Stackhouse Jr., D. J. McRae, and S. G. Conard (2004), Estimating fire emissions and disparities in boreal Siberia (1998–2002), *J. Geophys. Res.*, *109*, D14S06, doi:10.1029/2004JD004570.
- Soja, A. J., et al. (2009), Assessing satellite-based fire data for use in the National Emissions Inventory, *J. Appl. Remote Sens.*, *3*, 031504, doi:10.1117/1.3148859.
- Solomon, S., D. Qin, M. Manning, Z. Chen, M. Marquis, K. B. Averyt, M. Tignor, and H. L. Miller (Eds.) (2007), *Climate Change 2007: The Physical Science Basis: Contribution of Working Group I to the Fourth Assessment Report on the Intergovernmental Panel on Climate Change*, 996 pp., Cambridge Univ. Press, Cambridge, U. K.
- Streets, D. G., F. Yan, M. Chin, T. Diehl, N. Mahowald, M. Schultz, M. Wild, Y. Wu, and C. Yu (2009), Anthropogenic and natural contributions to regional trends in aerosol optical depth, 1980–2006, *J. Geophys. Res.*, *114*, D00D18, doi:10.1029/2008JD011624.
- Tosca, M. G., J. T. Randerson, C. S. Zender, D. L. Nelson, D. J. Diner, and J. A. Logan (2011), Dynamics of fire plumes and smoke clouds associated with peat and deforestation fires in Indonesia, *J. Geophys. Res.*, *116*, D08207, doi:10.1029/2010JD015148.
- Turquet, S., et al. (2007), Inventory of boreal fire emissions for North America in 2004: Importance of peat burning and pyroconvective injection, *J. Geophys. Res.*, *112*, D12S03, doi:10.1029/2006JD007281.
- Val Martin, M., J. A. Logan, R. A. Kahn, F.-Y. Leung, D. L. Nelson, and D. J. Diner (2010), Smoke injection heights from fires in North America: Analysis of 5 years of satellite observations, *Atmos. Chem. Phys.*, *10*, 1491–1510, doi:10.5194/acp-10-1491-2010.
- van der Werf, G. R., J. T. Randerson, L. Giglio, G. J. Collatz, and P. S. Kasibhatla (2006), Interannual variability in global biomass burning emission from 1997 to 2004, *Atmos. Chem. Phys.*, *6*, 3423–3441, doi:10.5194/acp-6-3423-2006.
- van der Werf, G. R., J. T. Randerson, L. Giglio, G. J. Collatz, M. Mu, P. S. Kasibhatla, D. C. Morton, R. S. DeFries, Y. Jin, and T. T. V. Leeuwen (2010), Global fire emissions and the contribution of deforestation, savanna, forest, agricultural, and peat fires (1997–2009), *Atmos. Chem. Phys.*, *10*, 11,707–11,735, doi:10.5194/acp-10-11707-2010.
- Vaughan, M., S. Young, D. Winker, K. Powell, A. Omar, Z. Liu, Y. Hu, and C. Hostetler (2004), Fully automated analysis of space-based lidar data: An overview of the CALIPSO retrieval algorithms and data products, *Proc. SPIE*, *5575*, 16–30, doi:10.1117/12.572024.
- Vermote, E., E. Ellicott, O. Dubovik, T. Lapyonok, M. Chin, L. Giglio, and G. J. Roberts (2009), An approach to estimate global biomass burning emissions of organic and black carbon from MODIS fire radiative power, *J. Geophys. Res.*, *114*, D18205, doi:10.1029/2008JD011188.
- Warneke, C., et al. (2009), Biomass burning in Siberia and Kazakhstan as an important source for haze over the Alaskan Arctic in April 2008, *Geophys. Res. Lett.*, *36*, L02813, doi:10.1029/2008GL036194.
- Werth, P., and R. Ochoa (1993), The evaluation of Idaho wildfire growth using the Haines index, *Weather Forecast.*, *8*, 223–234, doi:10.1175/1520-0434(1993)008<0223:TEOIWG>2.0.CO;2.
- Wiedinmyer, C., B. Quayle, C. Geron, A. Belote, D. McKenzie, X. Zhang, S. O'Neill, and K. K. Wynne (2006), Estimating emissions from fires in North America for air quality modeling, *Atmos. Environ.*, *40*, 3419–3432, doi:10.1016/j.atmosenv.2006.02.010.
- Wiedinmyer, C., S. K. Akagi, R. J. Yokelson, L. K. Emmons, J. A. Al-Saadi, J. J. Orlando, and A. J. Soja (2011), The Fire Inventory from NCAR (FINN): A high resolution global model to estimate the emissions from open burning, *Geosci. Model Dev.*, *4*, 625–641, doi:10.5194/gmd-4-625-2011.
- Winker, D. M., M. A. Vaughan, A. Omar, Y. Hu, K. A. Powell, Z. Liu, W. H. Hunt, and S. A. Young (2009), Overview of the CALIPSO mission and CALIOP data processing algorithms, *J. Atmos. Oceanic Technol.*, *26*, 2310–2323, doi:10.1175/2009JTECH1281.1.
- Winkler, J. A., B. E. Potter, D. F. Wilhelm, R. P. Shadbolt, K. Piromsopa, and X. Bian (2007), Climatological and statistical characteristics of the Haines Index for North America, *Int. J. Wildland Fire*, *16*, 139–152, doi:10.1071/WF06086.
- Wooster, M. J. (2002), Small-scale experimental testing of fire radiative energy for quantifying mass combusted in natural vegetation fires, *Geophys. Res. Lett.*, *29*(21), 2027, doi:10.1029/2002GL015487.
- Wooster, M. J., G. Roberts, G. L. W. Perry, and Y. J. Kaufman (2005), Retrieval of biomass combustion rates and totals from fire radiative power observations: FRP derivation and calibration relationships between biomass consumption and fire radiative energy release, *J. Geophys. Res.*, *110*, D24311, doi:10.1029/2005JD006318.
- Xiao-Peng, S., H. Chengquan, J. O. Sexton, F. Min, R. Narasimhan, S. Channan, and J. R. Townshend (2011), An assessment of global forest cover maps using regional higher-resolution reference data sets, paper presented at 2011 IEEE International Geoscience and Remote Sensing Symposium (IGARSS), IEEE, Vancouver, B. C., Canada, 24–29 July.
- Yu, H., et al. (2006), A review of measurement-based assessments of the aerosol direct radiative effect and forcing, *Atmos. Chem. Phys.*, *6*, 613–666, doi:10.5194/acp-6-613-2006.
- Zinke, P. J., A. G. Stangenberger, W. M. Post, W. R. Emanuel, and J. S. Olson (1986), Worldwide organic soil carbon and nitrogen data, *Rep. NDP-018*, Oak Ridge Natl. Lab., Oak Ridge, Ten., doi:10.2172/543663.